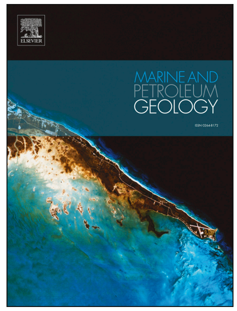

Geothermometry and geobarometry of overpressured lower Paleozoic gas shales in the Jiaoshiba field, Central China: Insight from fluid inclusions in fracture cements

Jian Gao, Sheng He, Jian-xin Zhao, Jizheng Yi

PII: S0264-8172(17)30064-8

DOI: 10.1016/j.marpetgeo.2017.02.018

Reference: JMPG 2825

To appear in: *Marine and Petroleum Geology*

Received Date: 19 October 2016

Revised Date: 6 February 2017

Accepted Date: 14 February 2017

Geothermometry and geobarometry of overpressured Lower Paleozoic gas shales in the Jiaoshiba field, Central China: Insight from fluid inclusions in fracture cements

Jian Gao[a], Sheng He [a,]*, Jian-xin Zhao[b], Jizheng Yi[c]

a Key Laboratory of Tectonics and Petroleum Resources of Ministry of Education, China University of Geosciences, Wuhan, 430074, China
b School of Earth and Environmental Sciences, University of Queensland, Brisbane QLD 4072, Australia
c SINOPEC Jianghan Oilfield Company, Qianjiang, 433124, China

Corresponding author: Sheng He shenghe@cug.edu.cn

Abstract: The Wufeng-Longmaxi organic-rich shales host the largest shale gas fields of China. This study examines sealed fractures within core samples of the Wufeng-Longmaxi shales in the Jiaoshiba shale gas field in order to understand the development of overpressures (in terms of magnitude, timing and burial) in Wufeng-Longmaxi shales and thus the causes of present-day overpressure in these Paleozoic shale formations as well as in all gas shales. Quartz and calcite fracture cements from the Wufeng-Longmaxi shale intervals in four wells at depth intervals between 2253.89 m and 3046.60 m were investigated, and the fluid composition, temperature, and pressure during natural fracture cementation determined using an integrated approach consisting of petrography, Raman spectroscopy and microthermometry. Many crystals in fracture cements were found to contain methane inclusions only, and aqueous two-phase inclusions were consistently observed alongside methane inclusions in all cement samples, indicating that fluid inclusions trapped during fracture cementation are saturated with a methane hydrocarbon fluid. Homogenization temperatures of methane-saturated aqueous inclusions provide trends in trapping temperatures that Th values concentrate in the range of 198.5 °C-229.9 °C, 196.2 °C-221.7 °C for quartz and calcite, respectively. Pore-fluid pressures of 91.8 to 139.4 MPa for methane inclusions, calculated using the Raman shift of C-H symmetric stretching (v_1) band of methane and equations of state for supercritical

methane, indicate fluid inclusions trapped at near-lithostatic pressures. High trapping temperature and overpressure conditions in fluid inclusions represent a state of temperature and overpressure of Wufeng-Longmaxi shales at maximum burial and the early stage of the Yanshanian uplift, which can provide a key evidence for understanding the formation and evolution of overpressure. Our results demonstrate that the main cause of present-day overpressure in shale gas deposits is actually the preservation of moderate-high overpressure developed as a result of gas generation at maximum burial depths.

Keywords: Fluid inclusions, Raman spectroscopy, Geobarometry, Wufeng-Longmaxi shales, Sichuan basin.

1. Introduction

A debate has centred around the overpressure found in various shale gas basins, with a particular focus on the cause of present-day overpressure in shale gas deposits. Two hypotheses were proposed to explain this phenomenon (Bowker, 2007). Hypothesis 1 suggests that the overpressured shales, which are both the reservoir and the source rock for the shale gas, are reentering the hydrocarbon-generation window now, regardless of the ongoing process of the uplift and exhumation of overburden rocks; Hypothesis 2 assumes the present-day overpressure is actually preserved from a normal pressure gradient (or slightly overpressured gradient formed by the generation of hydrocarbons at the time of maximum heat flow) established in the geologic past, and the extremely high capillary pressure of the shale allows the normal pressure to be preserved to achieve overpressures during the subsequent uplift and erosion of overburden rocks. Since Bowker (2007) first explained some irrationalities inherited in hypothesis 1, hypothesis 2 has become an increasingly more accepted model to account for the causes of present-day overpressures in shale gas deposits. In this paper, in order to test the above hypotheses 2, we performed fluid inclusions analysis and reconstructed the trapping time and associated temperature, pressure, and fluid-composition conditions. In contrast to hypotheses 2, we find that the present-day overpressure in the Wufeng-Longmaxi shales is actually preserved from moderate-high overpressure formed by the gas generation. This study has obtained some new insights into the causes of present-day overpressure in shale gas deposits as it applies to the Wufeng-Longmaxi shales as well to all gas shales.

As the first and largest producing shale gas field in China, more than 200 horizontal shale gas exploration wells have been drilled in the Wufeng-Longmaxi shales of the Jiaoshiba shale gas field, and it has the highest single-well daily shale gas production in China (Guo and Zhang, 2014). The marine shales within the Upper Ordovician Wufeng and Lower Silurian Longmaxi Formations, with estimated recoverable resources of up to 8.1×10^{12} m^3, have yielded about 50×10^{8} m^3 shale gas from 2012 to July, 2016. (Chen et al., 2015). Abnormally high pore-fluid pressures are widely developed in those high-yield shale gas wells, the gas reservoirs pressure coefficients range from 1.35 to 1.55 at the bottom of Wufeng-Longmaxi shales (Guo and Zhang, 2014). The overpressure is not only a favorable evidence for the long-term effective preservation conditions, but also a key factors for the enrichment of shale gas in Wufeng-Longmaxi shales. The scientific question that the relation between the preservation and enrichment of shale gas and the overpressure evolution in Wufeng-Longmaxi shales requires further study, and one of the basic research question is to find whether there is a direct and objective evidence of paleo-overpressure in Wufeng-Longmaxi shale gas reservoir. Fluid inclusion studies on fracture cements that formed concurrently with fracture opening have provided valuable information on the pressure and temperature of mineral growth at the time of the fluid migration and entrapment as well as on the compositions of the fluids involved in diagenesis in shale gas reservoirs (Becker et al., 2010; Fall et al., 2012 and 2015). During and after fluid migration in subsurface, including gas migration and entrapment in reservoirs, fluids may be encapsulated as inclusions during mineral precipitation (Parnell et al., 2001). Despite the problems of dealing with typically small and rare inclusions, and with the uncertainties involving extrapolation of the results from small fluid samples to a basin scale, fluid inclusions are particularly useful in determining (1) the temperature and pressure history (Burruss, 1989; Swarbrick, 1994; Aplin et al., 2000); (2) the timing of fluid migration/entrapment relative to the paragenesis (McLimans, 1987; Rezaee and Tingate, 1997) and the history of petroleum charge (Parnell, 2010); and (3) the evolution in pore-water salinity, which may be critical for evaluating the possible influence of fluid flow upon mineral cementation (Burley et al., 1989; Wilkinson et al., 1998).

In this contribution we present a study of fluid inclusions in sealed fractures from the Jiaoshiba shale gas field in the Sichuan Basin, which was designed to address the following questions: (1) how to obtain the trapping pressures of methane inclusions; (2) what is the initial state of pore-fluid pressure before tectonic uplift that is preserved in the present-day overpressure; and (3) What is the process responsible for the development of overpressures (in terms of magnitude, timing and burial) in gas shales. To achieve this goal, we combined basin modelling techniques with microthermometry and Raman microspectrometry of fluid inclusions trapped in the fracture minerals to constrain the fluid pressure, temperature and composition during fracture opening and cementation in the Jiaoshiba shale gas field. Trapping temperatures of fluid inclusions observed in fracture cements were correlated with independently derived burial history models to determine the relative timing of fracture opening. Fluid pressure conditions during fracture opening were determined based on gas concentration measurements in fluid inclusions and equation-of-state calculations. The present research adopt the approaches described in Lu et al. (2007a), Lin et al. (2007), Becker et al. (2010), and Fall et al. (2012; 2015), and builds on earlier diagenetic fracture cement fluid inclusion studies (Vrolijk et al., 1988; Goldstein and Reynolds, 1994; Worden et al., 1999; Eichhubl and Boles, 2000a; Parris et al., 2003; Hanks et al., 2006; Duncan et al., 2012).

2. Geological background

The Jiaoshiba shale gas field, located in the Fuling District of the Chongqing Municipality, is part of the Jiaoshiba structure of the Baoying-Jiaoshiba anticline in the eastern Sichuan fold belt (Figure 1A and B). The Jiaoshiba structure is controlled by two groups of faults trending in a North-East/South-West direction and a nearly north-south direction (Figure 1C), respectively. The main body of Jiaoshiba structure, which is a broad box-shaped faulted anticline with axial trending in NE, has tectonic stability and favorable preservation conditions (Guo and Zhang, 2014; Jin et al., 2015).

This study area has been affected by the Paleozoic Caledonian-Hercynian (541-251 Ma), Triassic Indosinian (251-201 Ma) and Jurassic-Cretaceous Yanshanian (201-65 Ma) and Cenozoic Himalayan (65-Present Ma) tectonic activities, which controlled the tectonic evolution of the southeast Sichuan Basin (Guo et al., 1996). The regional tectonic direction is NE, NNE (Figure 1B). Before late Cretaceous, the study area was mainly characterized by subsidence and minor uplift; while large scale tectonic compression and denudation caused by uplift occurred since late Cretaceous. Affected by the Yanshanian and Himalayan movement, most of the Jurassic-Quaternary sediments are eroded with only a thin set of Jurassic strata remaining in some areas (He et al., 2011; Yang et al., 2016). During the Late Ordovician to Early Silurian, the Caledonian orogeny reached its maximum, which placed the Upper Yangtze Platform under a compressional regime, resulting in the development of the Central, North and Qiangzhong Sichuan Uplifting Zones in the west, north and south of the Yangtze Platform (Liang et al., 2009; Zeng et al., 2012).

Due to the compression and development of several uplifting zones around the Sichuan Basin, the marine phase was reduced to restricted areas in the northeast, east and southeast Sichuan Basin during episodes of relative rising sea-level (Huang et al., 2011). At the same time, a relatively low energy, and anoxic environment was predominant in the southeast Sichuan Basin, which led to thick, organic rich shale being deposited in this area (Wang et al., 2009). During the Indosinian orogeny, the collision between the North China plat and the Yangtze plates occurred, resulting in the closure of the Paleo-Qinling ocean and termination of marine-phase deposition (Zhao et al., 2003). During the Late Yanshanian Orogeny, the study area experienced strong tectonic deformation, and a large scale thrust nappe developed in response to the continuous SE-NW compression initiated by the uplift of the Jiangnan-Xuefeng orogenic belt. The major basin-controlling faults of the study area possibly occurred in this period. During the Himalayan Orogeny, the long-range effects of the orogeny reactivated the early low-angle thrust faults, while the effects were much smaller than those in Late Yanshanian (He et al., 2011).

The black marine shales from the Upper Ordovician Wufeng Formation and the lower part of Lower Silurian Longmaxi Formation are the shale gas reservoirs in the Jiaoshiba shale gas field. The Lower Silurian Longmaxi Formation unconformably overlies the Ordovician Wufeng Formation, which comprises a set of thin siliceous shale and yields abundant Amplexograptus, Dicellograptus, Tangyagraptus and Diceratograptus (Chen et al., 1986, 2000, 2003, 2005). The organic-rich shales of the Wufeng-Longmaxi Formation represent deep to shallow shelf deposition. The high gas-bearing shales, which are composed of silica-rich carbonate and rich in graptolites and pyrites, mainly developed in deep shelf sedimentary environments (Guo et al., 2014). Drilling results show that organic-rich shales vary in thickness from 80 to 120 m, and the thickness of high gas-bearing shales is about 38-42 m. The organic-rich shales are divided into three layers and five sub-layers based on the characteristics of lithology, electric property, physical property, geochemistry, and the gas content. The high gas-bearing shales belong to layer 1 (Figure 2). The current burial depth of the shale gas reservoirs ranges from 2300 to 3500 m. The shale gas in the Wufeng-Longmaxi Formation is mainly composed of methane with a content range of 97.22%-98.47%. The contents of ethane and propane are 0.545%-0.801% and 0.05%-0.232%, respectively. The non-hydrocarbon components are low, and no H_2S is detected. The present-day shale gas reservoir temperature is around 82 ºC, the geothermal gradient is 2.72 ºC/100 m and the measured formation pressure and pressure coefficient of the gas reservoirs range from approximately 33.0 to 37.0 MPa, 1.35 to 1.55, respectively. The evolution histories of burial, thermal maturation and hydrocarbon generation of the Wufeng-Longmaxi Formation for well JY1 in the Jiaoshiba shale gas field were modelled and recalculated by He et al (2015) and Jin et al (2015).

3. Samples and analytical methods

Twenty samples of completely or partially cemented natural fractures in cores from wells JY1, JY11-4, JY41-5 and JY51-2 in the Wufeng-Longmaxi Formation at depths ranging from 2253.89 m to 3046.60 m were investigated. Of the twenty fracture samples that were screened, ten samples contained fluid inclusions large enough for microthermometry and Raman microprobe analyses. The locations of sampled wells and the details of these ten samples are shown in Figure 1 and Table 1. The core samples were prepared as thick doubly polished sections of approximately 100 μm thickness for fluid inclusion petrographic analysis, and Raman spectral and microthermometric measurements.

Fluid inclusion petrography and fluid inclusion assemblages were first examined using a NIKON-LV100 microscope equipped with both transmitted white and incident ultraviolet light (UV) sources. Microthermometry of methane inclusions and aqueous fluid inclusions was carried out using a calibrated

Linkam THM600 stage. Calibration and measurement routines have been described in earlier papers from our group (most recently in Guo et al., 2012). The homogenization temperatures (Th) and ice final melting temperatures (Tm) were obtained by cycling (Goldstein and Reynolds, 1994). Homogenisation temperature measurements were determined using a heating rate of 5 ºC/min. The final ice melting temperature measurements, which are dependent on the quantity of salt present in solution, were determined using a heating/cooling rate of 1 ºC/min. The measured temperature uncertainty for homogenization and ice melting temperatures are 0.1 ºC and 1 ºC, respectively. Stretched or leaked inclusions will yield homogenization temperatures (Th) greater than undeformed inclusions. To limit the possibility of unknowingly measuring deformed aqueous inclusions, only inclusions from the same field of view were measured during a single heating or freezing run. By restricting measurements to inclusions within the same field of view, any sudden changes in liquid/vapor ratios due to inclusion deformation could be observed and removed from consideration. Heating runs were conducted before freezing runs to reduce the possibility of inclusion stretching by freezing (Lawler and Crawford, 1983; Meunier, 1989). Where possible, only the smallest inclusions and/or those with rounded and smooth walls were measured as these should give the most reliable Th values (Ulrich and Bodner, 1988; Osborne and Haszeldine, 1993).

The Raman microprobe analyses of individual fluid inclusions were collected with a JY/Horiba LabRam HR800 Raman system equipped with a frequency doubled Nd:YAG laser (532.06 nm), whose output laser power is 45 mW, a 50× long-work-distance Olympus objective with 0.5 numerical aperture. The aperture of the confocal hole was set to 200 μm. Raman peak position calibration was verified regularly with the ~520.7 cm^{-1} band of a polished silicon wafer. The 300 grooves/mm grating was used to obtain spectra of the composition of fluid inclusions. Spectra were collected in the range of 0-4000 cm^{-1}. The acquisition time was around 100 seconds with two accumulations for each spectrum to maintain high signal-to-noise ratio. Three to five spectra were usually collected for each individual methane. The average values of the Raman peak position were used, although the deviations of the observations are generally very small (~1%) or undetectable. The 1800 grooves/mm grating was used to acquire spectra of the methane at room temperatures, for calculating the density in the inclusions with measured Raman shifts (Lu et al., 2007a). The emission lines of neon (Ne) laser at 2836.99 cm^{-1} (626.65 nm) and 3008.13 cm^{-1} (633.44 nm) were collected simultaneously with the Raman spectra. The method for calibration of methane peak positions described by Lin et al. (2007) was used. The accuracy of the peak position in wavenumber scale is ±0.2 cm^{-1}, resulting in an accuracy of ±0.01 g/cm^3 for density estimation.

Microthermometric measurements and Raman microprobe analyses have been made in the Key Laboratory of Tectonics and Petroleum Resources, China University of Geosciences in Wuhan.

BasinMod-1D (Version 7.06) software of Platte River Associates was used to reconstruct the burial and thermal histories by integrating the data of stratigraphic thickness, lithologies, absolute ages, erosion thickness, measured borehole temperatures and calculated vitrinite reflectance. Stratigraphic thickness and borehole temperature data were obtained from well completion reports supplied by the Jianghan Oilfield Company, Sinopec. Vitrinite reflectance data was derived from bitumen reflectance and FTIR characteristics of kerogen. The modelling process was mainly calibrated with vitrinite reflectance and temperatures.

4. Results

4.1 Fracture cement petrography

Fractures in the Wufeng-Longmaxi stratigraphic intervals were differentiated into two general types based on the mode of origin: joints and veins, naturally occurring planar vertical or subvertical fractures that do not exhibit any offset parallel to the fracture walls (Figure 3A); and faults, slickensided, horizontal to steeply dipping fractures (Figure 3B). The vast majority of the fracture types are joints and veins (Table 1). The joints and veins generally occur singly or less commonly as sets of closely spaced parallel fractures within the core. The slickensided fractures range in orientation from subhorizontal and bedding parallel, to inclined at 60 degrees to bedding. The slickensided surfaces are reflective, with very fine striations and, in some cases, deep grooves.

Fractures were mineralized with calcite as the predominant fracture cement in the Wufeng-Longmaxi stratigraphic intervals. Quartz cement were observed either as the only cement present, or as a cement phase postdating earlier calcite cement (Figure 3D and E). Quartz fracture cement consist of euhedral blocky crystals (Figure 3D). Calcite fracture cement occurred as banded columnar calcite, and as fine- to coarse-crystalline blocky calcite (Figure 3C). Almost all of the veins are filled with syntaxial mineral, which grows from both sides of the wall towards the median (i.e. symmetric) (Table 1). The vertical persistence of the fracture cement varies from a few to more than ten centimeters, whereas the vein width ranges from several millimeters to a maximum of 1.2 centimeters.

If minerals were stretched (deformed), their orientation of stretching relative to the wall of the vein was ascertained (Worden et al., 2016). The fabric of the deformed vein minerals is characterized as elongate (stretched) or hybrid elongate–blocky. The deformed vein minerals also show obvious lattice dislocation. Because no stretched microstructure and lattice dislocation were observed in the fractured samples, as well as most fractures in the Wufeng-Longmaxi shales are filled with blocky calcite and/or blocky quartz, the fractured samples in the Wufeng-Longmaxi stratigraphic intervals are undeformed rock samples. Each fracture opening increment was followed by a cement precipitation event that trapped fluid inclusions. Fluid inclusions occur as FIA (Fluid Inclusion Assemblages) representing a group of fluid inclusions that were all trapped at the same time (Figure 4), and allow interpretation of the fluid inclusion record of fluid temperature, pressure, and composition during fracture cementation.

4.2 Fluid inclusions

4.2.1 Fluid inclusion petrography

At room temperatures, the observed fluid inclusion assemblages (FIAs) in quartz are composed of two-phase aqueous inclusions and single-phase methane inclusions. Single-phase methane inclusions were observed in all samples that we analyzed, whereas most of the aqueous two-phase inclusions were consistently observed alongside methane inclusions (Figure 4 b and c). Many crystals in quartz cements were found to contain methane inclusions only (Figure 4 a, d and e). The coexistence of the methane inclusions and aqueous inclusions within the same fluid inclusion assemblage indicates inclusion trapping in the two-phase immiscible field (Goldstein and Reynolds, 1994), and that the aqueous inclusions are methane saturated. Both aqueous and methane inclusions have irregular or rounded shape, some methane inclusions even take negative crystal; The two-phase liquid-rich inclusions contain 5 to 10 vol. % vapor and range from <4 to 15μm in size. The single-phase methane inclusions are <6 to 30 μm in size (Figure 4). Most of the analyzed fluid inclusion assemblages in quartz that occur as being isolated or randomly distributed within the center of the euhedral cements, and are thus considered primary fluid inclusions, possibly having been trapped during crystal growth. Calcite cements also contain coexisting two-phase aqueous and single-phase methane inclusions, although both types of inclusions are much less abundant compared to quartz fracture cements. Inclusions in calcite are up to 8 μm in diameter with irregular to ellipsoidal shapes (Figure 4f).

4.2.2 Raman spectral analytical results of fluid inclusions

Raman spectroscopy is becoming a powerful tool for quantitative analysis of fluid inclusions in geochemical environments with various temperature, pressure, and salinity (Wopenka et al., 1990). After accurate calibration of Raman spectroscopic system, Raman shift of C-H symmetric stretching (v_1) band of methane can be applied to accurately calculate the pressure and density in individual fluid inclusions (Fabre and Couty, 1986; Ben-Amotz et al., 1992; Dubessy et al., 2001; Hansen et al., 2001; Lin et al., 2007; Lu et al., 2007a; Gao et al., 2015a).

Lu et al. (2007a) reported a unified cubic polynomial equation between the Raman CH_4 symmetric stretching (v_1) band shifts and the methane density:

$$\rho(g/cm^3) = -5.17331\times10^{-5}D^3 + 5.53081\times10^{-4}D^2 - 3.51387\times10^{-2}D \qquad \text{Eq.(1)}$$

with the correlation coefficient $r^2 = 0.9987$, where D (cm^{-1}) is the difference between the measured peak position of methane in fluid inclusion (v_{true}) and the known peak position of methane near zero pressure (v_0) ($D = v_{true}-v_0$). The lab reference shift v_0 for our laboratory is 2917.52 cm^{-1} (Zhang et al., 2015). The D–ρ relation is valid for pure CH_4 and CH_4–H_2O systems and for mixtures of CH_4 with low concentrations (<10 mol %) of other components (e.g., CO_2).

In this study, we used this D–ρ relation Eq.(1) to determine the density of methane inclusions, and then the trapping pressures of methane inclusions were calculated on the basis of this density and the homogenization temperatures of coexisting aqueous inclusions. Firstly, a 300 groove/mm grating and a spectral window of 0-3500 cm^{-1} by Raman spectroscopy were adopted to check the component of the single-phase fluid inclusions trapped in the quartz veins from wells JY11-4, JY41-5 and JY51-2, estimating whether the single-phase inclusions are suitable for Eq.(1). The results indicate that all analyzed single-phase fluid inclusions (a total of 151 single-phase fluid inclusions) from the eight quartz veins contain CH_4 as the only detectable phase during Raman analysis. Examination of the spectral regions where the most intense peaks for N_2, CO_2 and H_2S occur failed to detect any activity. The single-phase fluid inclusions, which are pure methane inclusions, are valid for the linear D–ρ relation Eq.(1). Secondly, the pure methane inclusions were studied with a 1800 groove/mm grating and a spectral window of 2750-3080 cm^{-1} to measure the C-H symmetric stretching (v_1) peak position of methane, calibrated with the neon lamp at room temperature (25 ºC). Using the unified equation (Eq.1), we calculated the density of these pure methane inclusions with the measured CH_4 symmetric stretching (v_1) band position.

Figure 5A gives two examples of Raman spectra of CH_4 in pure methane inclusions “a” and “b”. The measured methane peak positions were corrected using the Ne lamp reference shifts and the following equation (Lin et al., 2007): Using the measured peak positions for the CH_4 symmetric stretching band and the measured and real peak positions for the Ne 2836.99 and 3008.13 cm^{-1} lines, the corrected (true) position for the methane peak is given by the following expression:

$$v_{corr}^{CH_4} = \frac{1}{2}\{[v_{meas}^{CH_4} + (v_{real}^{Ne_1,2836.98} - v_{meas}^{Ne_1,2836.98})] + [v_{meas}^{CH_4} + (v_{real}^{Ne_2,3008.13} - v_{meas}^{Ne_2,3008.13})]\} \quad \text{Eq.(2)}$$

Thus, the measured CH_4 symmetric stretching (v_1) peak positions of 2907.79 cm^{-1}, 2908.13 cm^{-1} for pure methane inclusions “a” and “b” shown in Figure 5B correspond to a ‘‘true’’ or corrected peak position of 2911.11 cm^{-1} , 2911.45 cm^{-1} based on the linear interpolation described numerically by Eq.(2), respectively. Then the density of the methane inclusions can be calculated using the equation (1): The calculated D are -6.41 cm^{-1} and -6.07cm^{-1} for inclusions “a” and “b”, and the corresponding density are 0.262 and 0.245 g/cm^3, respectively. The range of the Raman CH_4 symmetric stretching (v_1) peak positions and the density of methane inclusions in each quartz veins from wells JY11-4, JY41-5 and JY51-2 in the Jiaoshiba shale gas field are listed in Table 2. The density of methane inclusions in each quartz vein are approximate, mainly ranging from 0.245 to 0.288 g/cm^3 (Table 2).

We also used the 300 groove/mm grating and a spectral window of 900~4100 cm^{-1} by Raman spectroscopy to check the component of two-phase aqueous inclusions, which are coexisting with pure methane inclusions (Figure 6). The results indicate that the aqueous inclusions are methane saturated and no ethane and/or carbon dioxide was detected in the aqueous inclusions. Measured homogenization temperatures of the aqueous fluid inclusions thus represent temperatures of inclusion trapping (Hanor, 1980).

4.2.3 Fluid inclusion microthermometry

Microthermometry results of methane inclusions

Microthermometry analytical technique can also be adopted to determine the density of methane inclusions (Roedder and Bodnar, 1980; Van den Kerkhof, 1990). While compared with the Raman spectroscopy technique, the microthermometry technique is time-consuming, and is usually difficult to be applied to small fluid inclusions (less than 5 μm), making determination of the density based on microthermometry difficult.

Homogenization temperatures of methane inclusions were measured for seven large inclusions in the studied fluid inclusion assemblages from sample JY11-4-1. Microthermometry of the single-phase methane inclusions indicates that the fluid in the inclusions is in the liquid state at room temperature, owing to the fact that the fluid inclusions nucleate a vapor bubble upon cooling. The inclusions homogenize to the liquid phase within the range of -95.8°C to -88.2 °C (Figure 7) (Gao et al., 2015a). This phase-change behavior indicates the presence of a fluid with density above the critical density of methane (Goldstein and Reynolds, 1994), indicating methane inclusions in the samples were trapped in a high density supercritical system. Homogenization temperatures below -82.1 °C (the critical temperature of methane) are indicative of pure methane inclusions (Andersen and Burke, 1996). The corresponding bulk density of the methane inclusions ranges from approximately 0.256 to 0.290 g/cm^3, which were calculated from the equation described by Liu et al (Liu and Shen, 1999).

Microthermometry results of aqueous inclusions

Aqueous inclusion assemblages (FIAs), which coexist with methane inclusions, hosted in quartz and calcite crystals from the Wufeng-Longmaxi Formation shale gas reservoir were selected for microthermometric analysis. Measured homogenization temperatures (Th), final ice-melting temperatures (Tm) and salinity data range are shown in Table 2, Table 3 and Figure 8, respectively.

The homogenization temperatures of aqueous inclusion assemblage in quartz cements throughout wells JY11-4, JY41-5 and JY51-2 mainly vary from 195.1 °C to 226.9 °C, 191.8 °C to 230.5 °C and 199.5 °C to 230.6 °C, respectively, with the average Th value of each FIA ranging from 198.5 °C to 229.9 °C. The Th values of aqueous inclusions in well JY51-2 are relatively higher than wells JY11-4 and JY41-5. These high homogenization temperatures are consistent with the fact that the Wufeng-Longmaxi shales were buried much deeper in this well. Details of each of these aqueous inclusion assemblages are given in Table 2. Several individual fluid inclusions in each FIA were measured to assess the reliability of observed homogenization temperatures. Th variation within individual FIAs in quartz are generally less than 8°C, suggesting that the inclusions were not re-equilibrated after trapping (Bodnar, 2003). The average Th value of each FIA is used to represent the trapping temperatures of coexisting methane inclusions in quartz cements. Most of these temperatures are well within the hydrocarbon gas-generation window of 105 to 220°C (Pepper and Corvi, 1995; Pepper and Dodd, 1995).

The homogenization temperatures of the fluid inclusions in calcite from well JY1 range from 196.0 °C to 245.8 °C, with Th variation of ~4-35 °C within a single fluid inclusion assemblage (Table 3). These larger temperature variations within individual fluid inclusion assemblages compared to inclusions in quartz are probably caused by partial re-equilibration of inclusions in calcite due to the low hardness and cleavage of the host mineral (Goldstein, 1986; Bodnar, 2003). While Th variation within ~4-8°C in several FIAs can be interpreted as suggesting that the inclusions were not re-equilibrated after trapping, and those Th values may represent the trapping temperatures of fluid inclusions in calcite cements.

Variability in the salinity of the aqueous fluid inclusions in a sample can indicate the trapping of palaeo-formation waters at different times. Initial and final ice-melting temperatures were generally difficult to observe due to the small size of the fluid inclusions. However, final ice-melting temperatures were measured for a few large inclusions in the studied fluid inclusion assemblages. Final ice-melting temperatures for inclusions were recorded in the range of approximately -3.7 to -9.8 °C in quartz throughout wells JY11-4 and JY41-5, corresponding to salinities of 6.01 to 13.72 °C wt. % NaCl equivalent (Figure 8). Final ice-melting temperatures for inclusions in calcite range from -3.1 to -5.3 °C, corresponding to salinities of 5.11 to 8.28 wt. % NaCl equivalent (salinity calculation based on Bodnar, 1993) (Table 3, Figure 8). The salinities show decreasing trends with increasing Th, with salinity variation within each sample varying by 0.35-5.86 wt. % NaCl equivalent (Figure 8). Since the Wufeng-Longmaxi shales clearly acted as closed overpressured systems (low permeability), the effect of external fluids is limited, and it is therefore plausible that the associated water with hydrocarbon generation and different degrees of water-rock reaction caused the salinity values of pore-filled water to shift toward lower values with temperature increase in the Wufeng-Longmaxi shales. The coexistence of aqueous inclusions and methane inclusions within indvidual fluid inclusion assemblages indicates the presence of a two-phase aqueous and methane-saturated fluid. Measured homogenization temperatures and salinities of the aqueous fluid inclusions thus represent fluid temperatures and salinities of inclusion trapping.

4.2.4 Isochore calculations and trapping pressure

Calculation of trapping pressure for fluid inclusions requires knowledge of the composition of the inclusions. Because it is difficult to find pure fluid inclusions of single component in naturally occurring minerals and the concentration of each component is hard to be determined in a multicomponent fluid inclusion, the calculation of trapping pressure for the fluid inclusions would not be precise. While based on the results of Raman spectroscopy analysis of methane inclusions from the Wufeng-Longmaxi shales in the Jiaoshiba shale gas field, we found pure methane inclusions, which are favourable for the calculation of trapping pressure.

The density of methane inclusions can be used to calculate fluid pressure during fracture opening and cementation. We followed the technique of Lu et al. (2007a) to determine the density within individual methane inclusions using Raman spectroscopic analyses. The fluid pressure at inclusion trapping conditions was calculated on the basis of the density of methane inclusions, homogenization temperature of coexisting aqueous inclusions, and the equation of state (EOS) for supercritical methane by Duan et al (1992).

The fluid pressure over a wide T-ρ range can be evaluated by the equation of state (Duan et al., 1992):

$$Z = \frac{PV}{RT} = \frac{P_r V_r}{T_r} = 1 + \frac{B}{V_r} + \frac{C}{V_r^2} + \frac{D}{V_r^4} + \frac{E}{V_r^5} + \frac{F}{V_r^2}\left(\beta + \frac{\gamma}{V_r^2}\right)\exp\left(-\frac{\gamma}{V_r^2}\right) \quad \text{Eq. (3).}$$

Where

$$B = a_1 + \frac{a_2}{T_r^2} + \frac{a_3}{T_r^3}; \quad \text{Eq. (4).}$$

$$C = a_4 + \frac{a_5}{T_r^2} + \frac{a_6}{T_r^3}; \quad \text{Eq. (5).}$$

$$D = a_7 + \frac{a_8}{T_r^2} + \frac{a_9}{T_r^3}; \quad \text{Eq. (6).}$$

$$E = a_{10} + \frac{a_{11}}{T_r^2} + \frac{a_{12}}{T_r^3}; \quad \text{Eq. (7).}$$

$$F = \frac{\alpha}{T_r^3}; \quad \text{Eq. (8).}$$

$$P_r = \frac{P}{P_c};$$ Eq. (9).

$$T_r = \frac{T}{T_c};$$ Eq. (10).

$$V_r = \frac{V}{V_c};$$ Eq. (11).

$$V_c = \frac{RT_c}{P_c};$$ Eq. (12).

Empirical parameters a_1-a_{12}, α, β, γ, Tc, and Pc in EOS for CH_4 are compiled by Duan et al. (1992). Tc is the critical temperature above which a gas cannot be liquefied by an increase in pressure. Pc is the minimum applied pressure required at the critical temperature to liquefy a gas. Vc is the volume of a fixed mass of fluid at Tc and Pc. V is the molar volume of fluid, calculated by molar mass and density of the fluid. Given the density of methane inclusions and the average homogenization temperature of coexisting aqueous inclusions, the trapping pressures can be calculated from equations (3)-(12).

Trapping pressures of methane inclusions range from approximately 91.8 to 139.4 MPa (Table 2) and are plotted in Figure 9 against estimated paleodepth. Also shown in Figure 9 are the hydrostatic gradient of 10.00 MPa/km and the lithostatic gradient of 24.99 MPa/km for comparison. The lithostatic gradient was calculated with a depth-averaged rock density of 2.55 g/cm^3, an estimate based on density-log data for the well JY1. The hydrostatic gradient was calculated for a water column with an average seawater density of 1.02 g/cm^3. Whereas most calculated trapping pressures plot at moderately high to near-lithostatic pressures, indicating pore-fluid pressures at the time of fracture opening significantly above the hydrostatic pressure gradient. Alternatively, or in addition, paleodepth estimation, which is based on a basin model (He et al., 2015; Jin et al., 2015), could be inaccurate because of the small variation in density estimations, leading to variations in the lithostatic gradient.

4.3 Basin model

Well JY1 was selected for simulating the burial, thermal and hydrocarbon generation histories (He et al., 2015). The burial history was modeled by back-stripping the present day sedimentary thickness of each stratigraphic unit chronologically with consideration of thickness changes by porosity-dependent decompaction, and the porosity-depth relationship for decompaction correction of Falvey and Middleton (1981) was adopted. The initial porosity and compaction factor of pure lithology (shale/mudstone, sandstone, siltstone and limestone) were adopted from the default values in the BasinMod software. Mixed lithologies were created by specifying percentages of the pure lithology for modeling of single well, and the mixed lithology properties (e.g. the initial porosity, compaction factor, density) were calculated by pure lithology properties. Present-day heat flow was calculated according to the thermal conductivities of the rock units and subsurface geothermal gradients, which are determined by the measured borehole temperatures. The transient heat flow model in the BasinMod 1D softwarewas was used to calculate the present-day heat flow. The calculated current heat flow value of the well JY1 are 45 mW/m^2. Based on the geological evolution of the eastern Sichuan fold belt, the modified Jarvis and Mckenzie (1980) algorithm for the rifting heat flow model was used to calculate the paleo-heat flows and assigned values that are typical for the evolution of superimposed basins (Lu et al., 2007; Zhu et al., 2010; Shi et al., 2012; Jiang et al., 2015). The good correlation between the modeled reflectance and temperature and the measured data implies that the thermal history model adopted is suitable for the study area (Figure 10). Maturity and hydrocarbon generation were calculated based on the Easy% Ro method proposed by Sweeney and Burnham (1990) and the NULL chemical kinetic model (Burnham et al., 1987), respectively. The kerogen type and initial TOC content were adopted according to actual geochemical results of the source rocks.

Figure 10 shows the reconstructed burial, thermal and hydrocarbon generation history for well JY1. The modeling result of well JY1 shows that oil generation from the O_3w-S_1l shales began from approximately 417 Ma with a temperature of 93 °C. The maturity of the O_3w-S_1l shales reached 0.7% Ro around 247 Ma and the peak of hydrocarbon generation (1.1% Ro) occurred at 210 Ma. The thermal maturity for the O_3w-S_1l shales reached 1.3% Ro at 182Ma (Early Jurassic), which are coincident with the end of the major oil generation stage. The phase of the thermal cracking into shale gas from the kerogen and liquid hydrocarbon in the O_3w-S_1l shales occurred during 182-85 Ma, including the dry gas window during the period of 145-85Ma. Since 85 Ma, the Yanshanian and Himalayan tectonic movements caused the formation uplift and erosion, the thermal evolution process of the O_3w-S_1l source rock tended to stop.

5. Discussion

5.1 Trapping conditions of fluid inclusions

We interpret trapping Th and pressures of fluid inclusions to represent trapping under methane saturation as the P-T conditions within the reservoir systematically change over time at maximum burial depth.

Single-phase methane inclusions were observed in all the samples that we analyzed, whereas aqueous two-phase inclusions were consistently observed alongside methane inclusions in several crystals of each sample, indicating that the pore fluid was saturated with methane and that a methane phase existed as a separate immiscible fluid phase at the time of the fractures formed. The separate immiscible phase of methane was in the supercritical state determined by the high density characteristic, and this absence of aqueous inclusions may reflect variations in gas saturation in the reservoir or, alternatively, in fluid-mineral wetting properties, resulting in preferential trapping of methane fluid in samples.

The coexistence of the methane and aqueous inclusions within the same fluid inclusion assemblage also indicates that fluid inclusions were trapped in the two-phase immiscible field (Roedder 1984; Goldstein and Reynolds, 1994). We infer aqueous inclusion trapping under water-saturated reservoir conditions that were in pressure communication with the supercritical methane phase. Pressure communication between these phases would ensure that any fluid inclusions trapped in the water phase would remain methane-saturated as P-T conditions declined in the reservoir during exhumation, and gas exsolved from the liquid phase (Becker et al., 2010). The presence of methane in the aqueous inclusions was confirmed by using Raman spectroscopy (Figure 6). We thus interpret these fluid inclusion temperatures and pressures as a record of the temperature and pressure evolution of the reservoir rather than variation in temperature caused by advective heat transport associated with episodic upward fluid flow.

Rapid upward fluid flow is necessary to obtain a locally perturbed temperature anomaly (Eichhubl and Boles, 2000b). In a reservoir of low matrix permeability, such flow conditions require a hierarchical network of well-connected fractures and faults found in some conventional fractured reservoirs (Eichhubl and Boles, 2000a). Such connected fracture systems are generally not characteristic of unconventional shale gas reservoirs that require hydraulic fracture stimulation to get a flow response in the wellbore.

5.2 Trapping time of fluid inclusions

The trapping time for methane inclusions can be estimated by combining fluid inclusion microthermometric data with burial and thermal history models obtained independently using burial and thermal maturity data, as was previously demonstrated by He et al. (2015) and Jin et al. (2015).

This basin history model predicts that the sampled core interval in well JY1 reached maximum burial conditions of 6263.5 m at around 85 Ma, with subsequent uplift to present depth of 2413.5 m (Figure 10). Maximum temperature conditions, predicted by He et al. (2015) based on present-day geothermal gradients and models of organic maturity evolution, are around 215°C for the stratigraphic horizon of sample JY1-1. Because temperature evolution models of well JY1 are not available for each well we sampled, we adapted the temperature evolution model of well JY1 for the sampled wells JY11-4, JY41-5 and JY51-2.

Temperature evolution were calculated for each sample by correcting measured depth to vertical depth and using the paleogeothermal gradient of 31.6 °C/km obtained from well JY1. All of these calculations assume a mean paleo-surface temperature of 18 °C, which agrees roughly with mean annual surface temperatures in the Yangtze region throughout the Cretaceous (Lu et al., 2007b; Shi et al., 2012). Predicted maximum temperature for the stratigraphic horizon of samples in wells JY11-4, JY41-5 and JY51-2 are around 214°C, 222°C and 239°C, respectively. This estimate compares well to the maximum homogenization temperatures of fluid inclusions in quartz fracture cements obtained independently in this study. This correspondence between the two estimates in maximum burial temperature confirms our interpretation that the fluid inclusion temperatures recorded the temperature evolution of the host rock rather than of pulses of hot upward moving fluid out of thermal equilibrium with the host rock.

A comparison of the fluid inclusion temperature trend from 199.8 °C to 221.4 °C in well JY11-4, 198.5 °C to 226.3 °C in well JY41-5, and 203.8 °C to 229.9 °C in well JY51-2 (Table 2) with burial and thermal maturity models, we infer that the trapping time of methane inclusions in the Wufeng-Longmaxi shales vary from 130 to 85 Ma, which indicates the fluid inclusions were trapped during maximum burial conditions and corresponding to the stage of petroleum cracking into dry gas. The general overlap in timing of trapping fluid inclusions and gas generation, in combination with the ubiquitous presence of methane inclusions and with high pore-fluid pressures calculated from fluid inclusion methane concentrations, is consistent with, though not necessarily indicative of, natural hydraulic fracturing driven by gas generation.

The larger Th variation within fluid inclusion assemblages in calcite (up to ~35 °C) compared to Th variations in quartz (less than 8 °C) suggests that some of the inclusions in calcite were stretched subsequent to trapping, resulting in homogenization temperatures that are elevated compared to inclusions unaffected by stretching (Goldstein and Reynolds, 1994; Bodnar, 2003). While the Th values in calcite obtained in several FIAs, whose Th variation is within ~4-8°C, are consistent with the lowest Th values obtained in the stretched FIAs. Thus, Th variation within ~4-8°C and the lowest Th values obtained in the stretched FIAs are interpreted to mean that the inclusions were not reequilibrated after trapping, and those Th values may represent the trapping temperatures of fluid inclusions in calcite cements. Thus, the trapping temperatures of fluid inclusion assemblages in calcite cements mainly vary from 196.2 °C to 221.7 °C. On the basis of a comparison of those Th values with burial and thermal maturity models, we infer that the fluid inclusions in calcite cements were also trapped during maximum burial conditions (Figure 10).

5.3 Paleo-pressure conditions in the shale gas reservoir

Fluid inclusion trapping temperatures and pressures represent a record of the temperature and pressure conditions of the Wufeng-Longmaxi Formation shale reservoir. Integrating the formation depth of quartz and calcite veins with the trapping pressures of fluid inclusion, the pressure state of the Wufeng-Longmaxi shales at maximum burial conditions can be confirmed.

Based on the geological data, the present-day formation pressure and pressure coefficients in the Wufeng-Longmaxi formation shale gas reservoir range from approximately 33.0 to 37.0 MPa, 1.35 to 1.55, respectively (Guo and Zhang, 2014; Jin et al., 2015). The present-day excess pressure (the difference between formation pressure and hydrostatic pressure) ranges from approximately 9.0 to 13.0 MPa. Our trapping-pressure estimates of fluid inclusions of 91.8 to 139.4 MPa indicate that paleo-pressure at maximum burial reached near-lithostatic pressures that are approximately triple as high as present-day values. According to the data of strata erosion thickness in the Jiaoshiaba shale gas field, which range from

3800 to 3850 m (He et al., 2015), we estimate the excess pressures of Wufeng-Longmaxi shales during maximum burial conditions range from approximately 33.9 to 83.6 MPa, and the pressure coefficients of Wufeng-Longmaxi shales during maximum burial conditions range from approximately 1.53 to 2.26 (Table 2), which indicates that Wufeng-Longmaxi shales were in the medium-to-high overpressure state at maximum burial and the early stage of the Yanshanian uplifting. The present-day overpressure in the Wufeng-Longmaxi Formation shale gas reservoir was actually preserved from medium-to-high overpressure state at the time of maximum burial depth. During uplift and exhumation, overpressure was continuously released to the present-day overpressure state.

The Wufeng-Longmaxi Formation is still overpressured at present, suggesting the Wufeng-Longmaxi shales remained closed systems during post-generation evolution of the shales and little gas loss (Hao et al., 2013). Due to closed fluid systems, much of the retained overpressures and gases were preserved, and the organic-rich Wufeng-Longmaxi shales have overpressures and high free gas contents at present. This allows the development of a schematic model for overpressure evolution in the Wufeng-Longmaxi shales to explain the process of preserving overpressure in the process of intensive tectonic uplift and erosion of overburden rocks. On the basis of the trapping pressure of methane inclusions, and the burial and thermal history of the Wufeng-Longmaxi shales, we used the equation of state (EOS) for CH_4 system by Duan et al. (1992) to simulate the pressure evolution of the Wufeng-Longmaxi shale gas reservoir during tectonic uplift and exhumation (Hanson and Lee, 2005; Gao et al., 2015b). Because the pores of the Wufeng-Longmaxi shales are completely compacted and dominant in nano-scale pore structure, and previous research also indicated that pore rebound of the Wufeng-Longmaxi shales is less than 2% after strata erosion thickness of 3850 m (Guo and Zhang, 2014), pore rebound of the Wufeng-Longmaxi shales in the process of tectonic uplift is limited and can be ignored. The main factors influencing the pressure changes in the Wufeng-Longmaxi shales are the temperature and the total gas content.

Our trapping-pressure estimates of fluid inclusion of 91.8 to 139.4 MPa indicate that the pressure coefficients at maximum burial ranged from approximately 1.53 to 2.26. Assuming that the initial uplift pressure coefficient was 1.7 and no gas loss in the process of tectonic uplift (the density of gas is constant), the present-day pressure coefficient calculated by EOS can reach the rupture limit of shales (Figure 11). Under this ideal conditions, we observe that the pressure is reduced as a result of the decreasing temperature in the process of tectonic uplift and exhumation, but pressure coefficient is increasing as a result of the erosion of overburden rocks (Figure 11). In order to retain the present-day pressure coefficient of 1.55, the diffusion of shale gas should reach approximately 24.9% of the total gas content of the initial state of tectonic uplift. The good preservation condition in Jiaoshiba shale gas field, the interaction of the extremely high capillary pressure of shale and the diffusion of gas permit medium-to-high overpressure at the early stage of the Yanshanian uplifting was continuously released to the present-day overpressure state.

6. Conclusions

Fluid inclusions trapped in quartz and calcite fracture-filling cement provide a record of fluid composition, temperature, and pressure during natural fracture cement, allowing tests of some of the fundamental aspects of the shale gas accumulation model, and the following conclusions can be drawn.

(1) Many crystals in fracture cements were found to contain methane inclusions only, and aqueous two-phase inclusions were consistently observed alongside methane inclusions in all cement samples, indicating that fluid inclusions trapped during fracture cement are saturated with a methane hydrocarbon fluid.

(2) Homogenization temperatures of methane-saturated aqueous fluid inclusions provide trends in trapping temperatures that Th values concentrate in the range of 198.5 °C-229.9 °C, 196.2 °C- 221.7 °C for quartz and calcite, respectively. Pore-fluid pressures of 91.8 to 139.4 MPa for methane inclusions, calculated using the Raman shift of C-H symmetric stretching (v_1) band of methane and equations of state for supercritical methane, indicate fluid inclusions trapped at near-lithostatic pressures. We interpret the high trapping temperature and overpressure conditions in fluid inclusions represent a state of temperature and overpressure of Wufeng-Longmaxi shales at maximum burial and the early stage of the Yanshanian uplift.

(3) On the basis of these microthermometric results and previously published thermal-maturation models, we infer that the trapping time of fluid inclusions occurred at 130-85 Ma. Independent estimates of dry gas generation in the Wufeng-Longmaxi shales overlap with the trapping of fluid inclusions in the Wufeng-Longmaxi Formation suggest that fluid overpressure have been generated during gas generation.

(4) Compared with the previous studies, our results demonstrate that the cause of present-day overpressure in shale gas deposits is actually preservation of moderate-high overpressure developed as a result of gas generation at maximum burial depth. The good preservation condition in Jiaoshiba shale gas field, the interaction of the extremely high capillary pressure of shale and the diffusion of gas permit some residual fluid overpressure were preserved to the present-day temperatures and pore-fluid pressures.

Acknowledgements

This work was supported by grant 41672139 from the National Natural Science Foundation of China and grant 2016ZX05005-001 from the National Key Scientific Special Project of China. Additional support was provided by grant 2016ZX05025002-003 from the thirteenth research plan of the Ministry of Science and Technology of China, grant 12120114046901 from the China Geological Survey, and a China

Scholarship Council (CSC) postgraduate award to Gao. We thank Zhiguo Shu for coordinating sample collection and data release, and Professor Wanjun Lu for Raman technical support. Our special thanks are extended to Associate Editor Johannes Wendebourg, as well as Professor R H Worden and two anonymous reviewers, for many critical and constructive comments.

References

Andersen, T., Burke, E.A., 1996. Methane inclusions in shocked quartz from the Gardnos impact breccia, South Norway. European Journal of Mineralogy 8, 927-936.

Aplin, A., Larter, S., Bigge, M., Macleod, G., Swarbrick, R., Grunberger, D., 2000. PVTX history of the North Sea's Judy oilfield. Journal of Geochemical Exploration 69, 641-644.

Becker, S., Eichhubl, P., Laubach, S., Reed, R., Lander, R., Bodnar, R., 2010. A 48 my history of fracture opening, temperature, and fluid pressure: Cretaceous Travis Peak Formation, East Texas basin. Geological Society of America Bulletin 122, 1081-1093.

Ben-Amotz, D., LaPlant, F., Shea, D., Gardecki, J., List, D., 1992. Raman Studies of Molecular Potential Energy Surface Changes in Supercritical Fluids. The Journal of Physical Chemistry 94, 1083-1047.

Bodnar, R., 1993. Revised equation and table for determining the freezing point depression of H_2O-NaCl solutions. Geochimica et Cosmochimica acta 57, 683-684.

Bodnar, R.J., 2003. Reequilibration of fluid inclusions. Fluid inclusions: Analysis and interpretation 32, 213-230.

Bowker, K.A., 2007. Barnett Shale gas production, Fort Worth Basin: issues and discussion. AAPG bulletin 91, 523-533.

Burley, S., Mullis, J.t., Matter, A., 1989. Timing diagenesis in the Tartan Reservoir (UK North Sea):

constraints from combined cathodoluminescence microscopy and fluid inclusion studies. Marine and Petroleum Geology 6, 98-120.

Burnham, A.K., Braun, R.L., Gregg, H.R., Samoun, A.M., 1987. Comparison of methods for measuring kerogen pyrolysis rates and fitting kinetic parameters. Energy & Fuels 1, 452-458.

Burruss, R.C., 1989. Paleotemperatures from fluid inclusions: advances in theory and technique, Thermal history of sedimentary basins. Springer, pp. 119-131.

Chen, L., Lu, Y., Jiang, S., Li, J., Guo, T., Luo, C., Xing, F., 2015. Sequence stratigraphy and its application in marine shale gas exploration: A case study of the Lower Silurian Longmaxi Formation in the Jiaoshiba shale gas field and its adjacent area in southeast Sichuan Basin, SW China. Journal of Natural Gas Science and Engineering.

Chen, X., Fan, J., Melchin, M., Mitchell, C., 2005. Hirnantian (latest Ordovician) graptolites from the Upper Yangtze region, China. Palaeontology 48, 235-280.

Chen, X., Melchin, M.J., Fan, J., Mitchell, C.E., 2003. Ashgillian graptolite fauna of the Yangtze region and the biogeographical distribution of diversity in the latest Ordovician. Bulletin de la Société Géologique de France 174, 141-148.

Chen, X., Qiu, J., 1986. Ordovician palaeoenvironmental reconstruction of Yichang area, W. Hubei. Journal of Stratigraphy 10, 1-15.

Chen, X., Rong, J., Charles, M., David AT, H., Fan, J., Zhan, R., Zhang, Y., Li, R., Wang, Y., 2000. Late Ordovician to earliest Silurian graptolite and brachiopod biozonation from the Yangtze region, South China, with a global correlation. Geological Magazine 137, 623-650.

Duan, Z., Møller, N., Weare, J.H., 1992. An equation of state for the CH_4-CO_2-H_2O system: I. Pure systems from 0 to 1000 °C and 0 to 8000 bar, Geochimica et Cosmochimica Acta, pp. 2605-2617.

Dubessy, J., Buschaert, S., Lamb, W., Pironon, J., Thiéry, R., 2001. Methane-bearing aqueous fluid inclusions: Raman analysis, thermodynamic modelling and application to petroleum basins. Chemical Geology 173, 193-205.

Duncan, A., Hanks, C., Wallace, W.K., O'Sullivan, P.B., Parris, T.M., 2012. An integrated model of the structural evolution of the central Brooks Range foothills, Alaska, using structural geometry, fracture distribution, geochronology, and microthermometry. AAPG bulletin 96, 2245-2274.

Eichhubl, P., Boles, J.R., 2000a. Focused fluid flow along faults in the Monterey Formation, coastal California. Geological Society of America Bulletin 112, 1667-1679.

Eichhubl, P., Boles, J.R., 2000b. Rates of fluid flow in fault systems; evidence for episodic rapid fluid flow in the Miocene Monterey Formation, coastal California. American Journal of Science 300, 571-600.

Fabre, D., Couty, R., 1986. Etude, par spectroscopie Raman, du méthane comprimé jusqu'à 3 kbar. Application à la mesure de pression dans les inclusions fluides contenues dans les minéraux. Comptes rendus de l'Académie des sciences. Série 2, Mécanique, Physique, Chimie, Sciences de l'univers, Sciences de la Terre 303, 1305-1308.

Fall, A., Eichhubl, P., Bodnar, R.J., Laubach, S.E., Davis, J.S., 2015. Natural hydraulic fracturing of tight-gas sandstone reservoirs, Piceance Basin, Colorado. Geological Society of America Bulletin 127, 61-75.

Fall, A., Eichhubl, P., Cumella, S.P., Bodnar, R.J., Laubach, S.E., Becker, S.P., 2012. Testing the basin-centered gas accumulation model using fluid inclusion observations: Southern Piceance Basin, Colorado. AAPG bulletin 96, 2297-2318.

Falvey, D., Middleton, M., 1981. Passive continental margins: evidence for a prebreakup deep crustal metamorphic subsidence mechanism. Oceanologica Acta 4, 103-114.

Gao, J., He, S., Yi, J., 2015a. Discovery of high density methane inclusions in Jiaoshiba shale gas field and its significance. Oil & Gas Geology 36, 472-480.

Gao, J., He, S., Zhao, M., 2015b. Gas Generation as the Dominant Overpressure Mechanism in Jiaoshiba Shale Gas Region, Sichuan Basin, China, AAPG International Conference & Exhibition, Melbourne, Australia.

Goldstein, R.H., 1986. Reequilibration of fluid inclusions in low-temperature calcium-carbonate cement. Geology 14, 792–795.

Goldstein, R.H., Reynolds, T.J., 1994. Systematics of fluid inclusions in diagenetic minerals: SEPM Short Course 31. Society for Sedimentary Geology, 199.

Guo, T., Zhang, H., 2014. Formation and enrichment mode of Jiaoshiba shale gas field, Sichuan Basin. Petroleum Exploration and Development 41, 31-40.

Guo, X., Hu, D., Li, Y., Liu, R., Wang, Q., 2014. Geological Features and Reservoiring Mode of Shale Gas Reservoirs in Longmaxi Formation of the Jiaoshiba Area. Acta Geologica Sinica (English Edition) 88, 1811-1821.

Guo, X., Liu, K., He, S., Song, G., Wang, Y., Hao, X., Wang, B., 2012. Petroleum generation and charge history of the northern Dongying Depression, Bohai Bay Basin, China: Insight from integrated fluid inclusion analysis and basin modelling. Marine and Petroleum Geology 32, 21-35.

Guo, Z., Deng, K., Han, Y., 1996. Formation and evolution of the Sichuan Basin. Geological Publishing House (in Chinese), Beijng.

Hanks, C., Parris, T., Wallace, W., 2006. Fracture paragenesis and microthermometry in Lisburne Group detachment folds: Implications for the thermal and structural evolution of the northeastern Brooks Range, Alaska. AAPG bulletin 90, 1-20.

Hanor, J., 1980. Dissolved methane in sedimentary brines; potential effect on the PVT properties of fluid inclusions. Economic Geology 75, 603-609.

Hansen, S.B., Berg, R.W., Stenby, E.H., 2001. Raman spectroscopic studies of methane-ethane mixtures as a function of pressure. Applied Spectroscopy 55, 745-749.

Hansom, J., Lee, M.K., 2005. Effects of hydrocarbon generation, basal heat flow and sediment compaction on overpressure development: a numerical study. Petroleum Geoscience 11, 353-360.

Hao, F., Zou, H., 2013. Cause of shale gas geochemical anomalies and mechanisms for gas enrichment and depletion in high-maturity shales. Marine and Petroleum Geology 44, 1-12.

He, Z., Wang, X., Li, S., Wo, Y., Zhou, Y., 2011. Yanshan Movement and its influence on petroleum preservation in middle-upper Yangtze region. Petroleum Geology & Experiment 1, 003.

He, S., Yi, J., Yang, R., Zhao, M., 2015. Modeling of Evolution Histories of Thermal Maturity and Hydrocarbon Generation for the Lower Paleozoic Black Marine Shales in Jiaoshiba Region of Sichuan Basin, China. AAPG International Conference & Exhibition, Melbourne, Australia.

Huang, W., Liu, S., Ma, W., Wang, G., Zeng, X., Wang, J., 2011. Shale gas exploration prospect of Lower Paleozoic in southeastern Sichuan and western Hubei-eastern Chongqing areas, China. Geological Bulletin of China 30, 364-371.

Jarvis, G.T., Mckenzie, D.P., 1980. Sedimentary basin formation with finite extension rates. Earth Planetary Science Letters 48, 42-52.

Jiang, Q., Zhu, C.q., Qiu, N.S., Cao H.y., 2015. Paleo-heat Flow and Thermal Evolution of the Lower Cambrian Qiongzhusi Shale in the Southern Sichuan Basin, SW China. Natural Gas Geoscience 26, 1563-1570.

Jin, Z., Li, M., Hu, Z., Gao, B., Nie, H., Zhao, J., 2015. Shorten the Learning Curve Through

Technological Innovation: A Case Study of the Fuling Shale Gas Discovery in Sichuan Basin, SW China. Unconventional Resources Technology Conference (URTEC), San Antonio, Texas, USA.

Lawler, J.P., Crawford, M.L., 1983. Stretching of fluid inclusions resulting from a low-temperature microthermometric technique. Economic Geology 78, 527–529.

Liang, D., Guo, T., Bian, L., Chen, J., Zhao, Z., 2009. Some progresses on studies of hydrocarbon generation and accumulation in marine sedimentary regions, southern China (Part 3): Controlling factors on the sedimentary facies and development of Palaeozoic marine source rocks. Marine Origin Petroleum Geology 2, 003.

Lin, F., Bodnar, R., Becker, S., 2007. Experimental determination of the Raman CH_4 symmetric stretching (v_1) band position from 1-650 bar and 0.3-22 °C: Application to fluid inclusion studies. Geochimica et Cosmochimica Acta 71, 3746-3756.

Liu, B., Shen, K., 1999. The thermodynamic simulation of fluid inclusions. Geological Publishing House (in Chinese), Beijing.

Lu, Q.Z., Ma, Y.S., Guo, T,L., Hu, S,B., 2007. Thermal history and hydrocarbon generation history in Western Hubei-eastern Chongqing area. Chinese Journal of Geology 42, 189-198.

Lu, W., Chou, I., Burruss, R., Song, Y., 2007a. A unified equation for calculating methane vapor pressures in the CH_4-H_2O system with measured Raman shifts. Geochimica et Cosmochimica Acta 71, 3969-3978.

Lu, Q.Z., Ma, Y.S., Guo, T,L., Hu, S,B., 2007b. Thermal history and hydrocarbon generation history in Western Hubei-eastern Chongqing area. Chinese Journal of Geology 42, 189-198.

McLimans, R.K., 1987. The application of fluid inclusions to migration of oil and diagenesis in petroleum reservoirs. Applied Geochemistry 2, 585-603.

Meunier, J.D., 1989, Assessment of low-temperature fluid inclusions in calcite using microthermometry.

Economic Geology 84, 167–170.

Osborne, M., Haszeldine, S., 1993. Evidence for resetting of fluid inclusion temperatures from quartz cements in oilfields. Marine and Petroleum Geology 10, 271-278.

Ozkan, A., Cumella, S.P., Milliken, K.L., Laubach, S.E., 2011. Prediction of lithofacies and reservoir quality using well logs, late cretaceous williams fork formation, mamm creek field, piceance basin, colorado. AAPG bulletin 95, 1699-1723.

Parnell, J., 2010. Potential of palaeofluid analysis for understanding oil charge history. Geofluids 10, 73-82.

Parnell, J., Middleton, D., Honghan, C., Hall, D., 2001. The use of integrated fluid inclusion studies in constraining oil charge history and reservoir compartmentation: examples from the Jeanne d'Arc Basin, offshore Newfoundland. Marine and Petroleum Geology 18, 535-549.

Parris, T., Burruss, R., O'Sullivan, P., 2003. Deformation and the timing of gas generation and migration in the eastern Brooks Range foothills, Arctic National Wildlife Refuge, Alaska. AAPG bulletin 87, 1823-1846.

Pepper, A.S., Corvi, P.J., 1995. Simple kinetic models of petroleum formation. Part 1: Oil and gas generation form kerogen. Marine and Petroleum Geology 12, 291–319.

Pepper, A. S., Dodd, T.A., 1995. Simple kinetic models of petroleum formation. Part 2: Oil-gas cracking. Marine and Petroleum Geology 12, 321–340.

Rezaee, M.R., Tingate, P.R., 1997. Origin of quartz cement in the Tirrawarra sandstone, southern Cooper basin, South Australia. Journal of Sedimentary Research 67, 168-177.

Roedder, E., Bodnar, R., 1980. Geologic pressure determinations from fluid inclusion studies. Annual Review of Earth and Planetary Sciences 8, 263.

Roedder, E., 1984, Fluid Inclusions: Washington, D.C., Mineralogical Society of America, 644.

Shi, H.C., Shi, X.B., Yang, X.Q., Jiang, H.Y., Long, Y.K., 2012. Exhumation process of the Fangdoushan-Shizhu fold belt in Meso-Neozoic and its tectonic significance in Western Hubei-Eastern Chongqing. Progress in Geophysics 26, 1993-2002.

Stroker, T.M., Harris, N.B., Elliott, W.C., Wampler, J.M., 2013. Diagenesis of a tight gas sand reservoir: Upper cretaceous mesaverde group, Piceance Basin, Colorado. Marine and Petroleum Geology 40, 48-68.

Swarbrick, R., 1994. Reservoir diagenesis and hydrocarbon migration under hydrostatic palaeopressure conditions. Clay Minerals 29, 473-474.

Sweeney, J.J., Burnham, A.K., 1990. Evaluation of a simple model of vitrinite reflectance based on chemical kinetics. AAPG Bulletin 74, 1559-1570.

Ulrich, M.R., Bodner, R.J., 1988. Systematics of stretching of fluid inclusions II: Barite at 1 atmosphere confining pressure. Economic Geology 83, 1037–1046.

Van den Kerkhof, A., 1990. Isochoric phase diagrams in the systems CO_2-CH_4 and CO_2-N_2: Application to fluid inclusions. Geochimica et Cosmochimica Acta 54, 621-629.

Vrolijk, P., Myers, G., Moore, J.C., 1988. Warm fluid migration along tectonic melanges in the Kodiak accretionary complex, Alaska. Journal of Geophysical Research: Solid Earth (1978–2012) 93, 10313-10324.

Wang, S., Wang, L., Huang, J., Li, X., Li, D., 2009. Silurian shale gas forming conditions on the Yangtze area. Natural Gas Industry 29, 45-50.

Wilkinson, J., Lonergan, L., Fairs, T., Herrington, R., 1998. Fluid inclusion constraints on conditions and timing of hydrocarbon migration and quartz cementation in Brent Group reservoir sandstones, Columba Terrace, northern North Sea. Geological Society, London, Special Publications 144, 69-89.

Worden, R.H., Benshatwan, M.S., Potts, G.J., Elgarmadi, S.M., 2016. Basin-scale fluid movement patterns revealed by veins: Wessex Basin, UK. Geofluids 16, 149-174.

Worden, R.H., Coleman, M.L., Matray, J.M., 1999. Basin scale evolution of formation waters: a diagenetic and formation water study of the Triassic Chaunoy Formation, Paris Basin. Geochimica et Cosmochimica Acta 63, 2513-2528.

Wopenka, B., Pasteris, J.D., Freeman, J.J., 1990. Analysis of individual fluid inclusions by Fourier transform infrared and Raman microspectroscopy. Geochimica et Cosmochimica Acta 54, 519-533.

Yang, R., He, S., Hu, Q., Hu, D., Zhang, S., Yi, J., 2016. Pore characterization and methane sorption capacity of over-mature organic-rich Wufeng and Longmaxi shales in the southeast Sichuan Basin, China. Marine and Petroleum Geology 77, 247-261.

Zeng, X., Liu, S., Huang, W., Zhang, C., 2012. Comparison of Silurian Longmaxi Formation shale of Sichuan Basin in China and Carboniferous Barnett Formation shale of Fort Worth Basin in United States. Geological Bulletin of China 30, 273-384.

Zhang, J., Qiao, S., Lu, W., Hu, Q., Chen, S., LIU, Y., 2015. A unified equation for determining methane densities in fluid inclusions with measured Raman shifts. Journal of Geochemical Exploration.

Zhao, Z., Yu, G., Zhu, Y., 2003. Tectonic evolution and its control over hydrocarbon in southern China. Journal of Chengdu University of Technology 30, 155-168.

Zhu C.Q., Xu, M., Yuan Y.S., Zhao, Y.Q., 2010. Palaeo-geothermal response and record of the effusing of Emeishan basalts in Sichuan basin. Chinese Sci Bull 55, 474-482.

Figure Captions

Figure 1. (A) and (B) Location map of the study area showing the sub-tectonic units of the eastern part of Sichuan Basin; (C) Distribution of the Jiaoshiba shale gas field and faults within gas field with the locations of representative sampled wells.

Figure 2. Stratigraphic column of the Upper Ordovician-Lower Silurian of well JY1 in Jiaoshiba shale gas field, showing sedimentary facies evolution stages and the thickness and TOC content of high gas-bearing organic-rich shales.

Figure 3. Photomicrograph of quartz and calcite veins under transmitted light hosted in marine organic-rich shales in Jiaoshiba shale gas field: (A) Core photo shows the fracture type is joint that do not exhibit any offset parallel to the fracture walls (Sample JY41-5-3, Wufeng Formation, measured depth 2616.71 m); (B) Core photo shows the fracture type is the slickensided fracture, and the slickensided surface is reflective (Sample JY41-5-2, Longmaxi Formation, measured depth 2526.45 m); (C) Fracture in C is completely cemented by blocky calcite veins (Sample JY11-4-3, Longmaxi Formation, measured depth 2339.22 m); (D) Fracture in D is a crack-seal composite vein, which is partially cemented by blocky quartz in the interior of the fracture and partially cemented by blocky sparry calcite in the each wall of the fracture (Sample JY41-5-3, Wufeng Formation, measured depth 2616.71 m); (E) Photomicrograph mosaic of a thick composite vein section illustrating the relative timing of fracture cements in the Wufeng-Longmaxi Formation (Sample JY41-5-3, Wufeng Formation, measured depth 2616.71 m).

Figure 4. Photomicrographs under transmitted light of representative methane inclusions and the coexisting

aqueous inclusions in quartz and calcite veins from wells JY11-4, JY41-5, JY51-2 and JY1 in the Jiaoshiba shale gas field. (a) and (b): Representative methane inclusions and the coexisting aqueous inclusions were trapped in quartz veins from the sample JY11-4-1 (Longmaxi Formation, measured depth 2253.89 m); (c) and (d): Representative methane inclusions and the coexisting aqueous inclusions were trapped in quartz veins from the sample JY41-5-2 (Wufeng Formation, measured depth 2526.45 m); (e): Methane inclusions were trapped in quartz veins from the sample JY41-5-3 (Wufeng Formation, measured depth 2616.71 m); (f): Representative methane inclusions and the coexisting aqueous inclusions were trapped in calcite veins from the sample JY1-1 (Wufeng Formation, measured depth 2413.50 m).

Figure 5. (A) Laser Raman spectra collected from pure methane inclusions “a” and “b” with 300 groove/mm grating. (B) Laser Raman spectra of CH_4 in pure methane inclusions “a” and “b” with 1800 groove/mm grating. Ne_1 and Ne_2 are two bands corresponding to the Ne lamp scattering bands of 2836.99 cm^{-1} and 3008.13 cm^{-1}, respectively. Fluid inclusion “a” was trapped in the sample JY11-4-1 (Longmaxi Formation, measured depth 2253.89 m), and fluid inclusions “b” were trapped in the sample JY41-5-4 (Wufeng Formation, measured depth 2619.83 m).

Figure 6. Laser Raman spectra of dissolved CH_4 in the aqueous phase of inclusion “c”. Fluid inclusion “c” were trapped in the sample JY41-5-4 (Wufeng Formation, measured depth 2619.83 m).

Figure 7. Micrographs of phase transition processes during determination of homogenization temperatures for methane inclusions from well JY11-4-1 in the Jiaoshiba shale gas field. (a), (d) Micrographs showing individual methane inclusions at 20.0℃ before temperature determination on microscope heating stage; (b)

Micrograph for vapor bubble formation in a methane inclusion at -103.8℃; (c) Micrograph for vapor bubble disappearance from the same methane inclusion as in (b) at Th = -95.1℃; (e) Micrograph for vapor bubble formation in another methane inclusion at -98.8℃, (f) Micrograph for vapor bubble disappearance from the same methane inclusion as in (e) at Th = -88.6℃.

Figure 8. Cross plot of homogenization temperature and salinity of aqueous inclusions coeval with methane inclusions from the Wufeng-Longmaxi Formation shale gas reservoir units. Note that the salinities show decreasing trends with increasing Th, with salinities variation within each sample varying by 0.35-5.86 wt. % NaCl equivalent.

Figure 9. Calculated trapping pressures plotted against inferred maximum burial depth, including an estimated 3850 m of Cenozoic section removed by erosion in the last 85 Ma in the Sichuan Basin.

Figure 10. Burial history, thermal history and hydrocarbon generation evolution modeling of the Wufeng-Longmaxi Formation in well JY1, showing the approximate trapping times of the aqueous inclusions vary from 130 to 85 Ma.

Figure 11. The simulative pressure evolution of the Wufeng-Longmaxi shales under ideal conditions that no gas loss in the process of tectonic uplift and erosion. Assuming that the initial uplift pressure coefficient is 1.7 and no gas loss in the process of tectonic uplift, the main factor influencing the pressure changes under this ideal conditions is the formation temperature, thus the present-day pressure coefficient can reach the rupture limit of shales.

Table Captions

Table 1. Details of shale samples containing quartz and calcite veins selected from wells JY1, JY11-4, JY41-5 and JY51-2 for fluid inclusion analysis in Jiaoshiba shale gas field, Sichuan Basin. Samples investigated in this study include location, depth, stratigraphic position, host lithology, fracture orientation, fracture type, width and length of fracture, types of mineral growth pattern, morphology of crystals and the mineral phase of the fracture fill.

Table 2. Raman CH_4 symmetric stretching (v_1) peak position, calculated density, measured aqueous FI Th, and reconstructed trapping pressure of methane inclusions in quartz fracture cements in the Jiaoshiba shale gas field.

Table 3. Measured Th of aqueous fluid inclusions in calcite cements from well JY1 in the Jiaoshiba shale gas field.

Table 1. Details of shale samples containing quartz and calcite veins selected from wells JY1, JY11-4, JY41-5 and JY51-2 for fluid inclusion analysis in Jiaoshiba shale gas field, Sichuan Basin. Samples investigated in this study include location, depth, stratigraphic position, host lithology, fracture orientation, fracture type, width and length of fracture, types of mineral growth pattern, morphology of crystals and the mineral phase of the fracture fill.

Location	Sample	Depth (m)	Stratigraphy	Host lithology	Orientation	Fracture type	Width/ length of fracture (cm)	Vein fill relative to median	Morphology of crystals in vein	Dominant mineralogy of vein
JY1	JY1-1	2413.50	Wufeng Formation	Silica-rich carbonaceous shales	Horizontal	Slickensided	0.3/None	Syntaxial (symmetric)	hybrid elongate-blocky	Calcite
JY11-4	JY11-4-1	2253.89	Longmaxi Formation	Turbidite siltstone	Sub-vertical	joints and veins	0.4/15	Syntaxial (symmetric)	Blocky	Quartz
	JY11-4-2	2319.76	Longmaxi Formation	Carbonaceous siltstone	Horizontal	joints and veins	0.4/None	Syntaxial (symmetric)	Blocky	Quartz+Calcite
	JY11-4-3	2339.22	Longmaxi Formation	Silica-rich carbonaceous shales	Sub-vertical	joints and veins	0.2/12	Syntaxial (symmetric)	Blocky	Calcite
JY41-5	JY41-5-1	2508.11	Longmaxi Formation	Turbidite siltstone	High angle	joints and veins	0.4/20	Syntaxial (symmetric)	Blocky	Quartz
	JY41-5-2	2526.45	Longmaxi Formation	Silty shales	Sub-horizontal	Slickensided	0.2/None	Syntaxial (unitaxial)	Blocky	Quartz
	JY41-5-3	2616.71	Wufeng Formation	Silica-rich carbonaceous shales	High angle	joints and veins	0.3/None	Syntaxial (symmetric)	Blocky	Quartz+Calcite
	JY41-5-4	2619.83	Wufeng Formation	Silica-rich carbonaceous shales	High angle	joints and veins	0.1/14	Syntaxial (symmetric)	Blocky	Quartz
JY51-2	JY51-2-1	3037.50	Longmaxi Formation	Turbidite siltstone	Sub-vertical	joints and veins	0.4/None	Syntaxial (symmetric)	Blocky	Quartz
	JY51-2-2	3046.60	Longmaxi Formation	Turbidite siltstone	Sub-vertical	joints and veins	12/None	Syntaxial (symmetric)	Blocky	Quartz

Table 2. Raman CH_4 symmetric stretching (v_1) peak position, calculated density, measured aqueous FI Th, and reconstructed trapping pressure of methane inclusions in quartz fracture cements in the Jiaoshiba shale gas field

Sample	Depth (m)	v_{corr} of methane inclusions (cm^{-1})	Measured number of methane inclusions	Calculated density of methane inclusions (g/cm^3)	Th of coexisting aqueous inclusions (range and mean) (℃)		Measured number of aqueous inclusions	Reconstructed trapping Pressure (MPa)	Pressure coefficients
Well JY11-4									
JY11-4-1	2253.89	2910.7583-2910.7603	3	0.279	217.5-219.3	218.4	2	126.2-126.3	2.08
		2910.5711-2911.2660	5	0.254-0.288	214.7-225.9	220.3	5	130.9-137.1	2.16-2.26
		2910.7583-2911.1055	4	0.262-0.279	195.1-203.8	199.8	4	104.0-119.5	1.72-1.97
		2910.7583-2910.9185	2	0.271-0.279	-	-	-	-	-
		2910.7603-2911.1055	3	0.262-0.279	201.6-206.9	203.7	4	105.2-120.9	1.74-2.0
		2910.7603-2911.1072	4	0.262-0.279	201.8-206.4	204.2	3	105.3-121.1	1.73-2.0
		2910.9337-2911.1072	5	0.262-0.270	198.8-203.7	201.3	2	104.4-111.9	1.72-1.85
JY11-4-2	2319.76	2911.1072-2911.4544	3	0.245-0.262	204.1-214.7	209.7	6	93.6-107.1	1.53-1.75
		2910.7603-2911.1072	4	0.262-0.279	217.4-225.1	221.4	3	110.9-127.3	1.81-2.08
		2910.9187-2911.2661	5	0.254-0.271	-	-	-	-	-
		2910.9185-2911.2659	4	0.254-0.272	215.8-226.9	219.6	4	103.7-118.9	1.69-1.94
Well JY41-5									
JY41-5-1	2508.11	2911.1072-2911.4544	6	0.245-0.262	216.2-223.7	219	4	96.2-110.1	1.53-1.75
		2911.1075-2911.4544	4	0.245-0.262	222.9-230.1	226.3	3	98.3-112.4	1.56-1.78
		2911.2809-2911.4544	3	0.245-0.253	-	-	-	-	-
		2911.1482	2	0.260	-	-	-	-	-
		2910.7603-2911.1075	3	0.262-0.279	207.6-216.9	210.7	5	107.4-123.4	1.70-1.95
		2911.1075-2911.4544	3	0.245-0.262	-	-	-	-	-
		2911.1072-2911.1075	4	0.262	206.9-208.5	207.9	4	106.5	1.69
JY41-5-2	2526.45	2910.7603-2911.1072	4	0.262-0.279	207.9-218.4	212.1	3	107.9-123.9	1.71-1.96
		2910.4798-2910.7603	3	0.279-0.293	196.8-203.1	198.5	5	119.0-133.6	1.88-2.11
		2910.7603-2910.9337	3	0.270-0.279	-	-	-	-	-
		2910.7603-2911.4542	4	0.245-0.279	213.3-222.6	217.6	5	95.8-125.9	1.51-1.99
		2911.1055-2911.2806	3	0.253-0.262	217.3-221.8	218.9	3	102.8-110.1	1.63-1.74
		2910.7603-2911.1072	2	0.262-0.279	-	-			

JY41-5-3	2616.71	2910.7256-2911.4399	3	0.246-0.281	220.8-224.2	221.9	5	97.6-129.3	1.52-2.01
		2910.9186-2911.2661	5	0.254-0.271	214.8-218.9	216.6	4	102.7-117.8	1.60-1.84
		2911.0925-2911.6135	4	0.238-0.262	-	-	-	-	-
		2910.9187-2911.6135	4	0.238-0.271	214.3-230.5	223.6	5	91.8-120.2	1.43-1.87
		2910.5712	1	0.288	180.6-182.9	181.8	2	122.0	1.91
JY41-5-4	2619.83	2911.1072-2911.2806	4	0.253-0.262	224.4-230.3	226.3	7	105-1-112.4	1.63-1.75
		2910.7603-2911.1072	4	0.262-0.279	191.8-203.2	199.2	7	103.7-119.2	1.61-1.85
		2910.9187-2911.4399	4	0.246-0.271	215.8-218.7	217.4	4	96.3-118.1	1.50-1.83
		2910.5712-2911.2662	3	0.254-0.288	205.9-219.7	212.8	5	101.6-134.2	1.58-2.09
Well JY51-2									
JY51-2-1	3037.50	2910.9186-2911.2660	6	0.254-0.271	220.3-228.5	225.7	4	105.5-120.9	1.54-1.77
		2910.5712	4	0.288	208.9-217.8	212.8	3	116.5-134.2	1.70-1.96
		2910.9187-2911.0923	2	0.263-0.271	223.8-230.6	228.5	5	113.8-121.9	1.66-1.78
		2910.9187-2911.2661	3	0.254-0.271	229.9	229.9	1	106.7-122.4	1.56-1.79
JY51-2-2	3046.60	2910.7641-2911.1110	8	0.262-0.279	-	-	-	-	-
		2910.4172-2910.7641	4	0.279-0.296	199.5-208.4	203.8	3	120.7-139.4	1.76-2.03
		2910.7643-2911.1110	5	0.262-0.279	216.8-225.1	222.3	6	110.9-127.4	1.61-1.86
		2910.7641-2910.9376	3	0.270-0.279	214.3-217.9	214.9	3	116.3-124.8	1.70-1.82

Table 3. Measured Th of aqueous fluid inclusions in calcite cements from well JY1 in the Jiaoshiba shale gas field

Sample	Depth /m	FIA	Number	Th/℃	Tm/℃	Salinity (wt.%) NaCl Equivalent
Well JY1	2413.5	FIA-1	6	196.2-202.4		
		FIA-2	5	196.0-204.7	-3.9~-4.1	6.30~6.59
		FIA-3	5	201.6-238.4		
		FIA-4	4	207.5-214.8	-3.8~-4.2	6.16~6.74
		FIA-5	3	213.5-217.4	-3.6~-3.8	5.86~6.16
		FIA-6	5	214.8-236.0		
		FIA-7	4	217.6-245.8	-3.1~-5.3	5.11~8.28
		FIA-8	6	215.8-239.7		

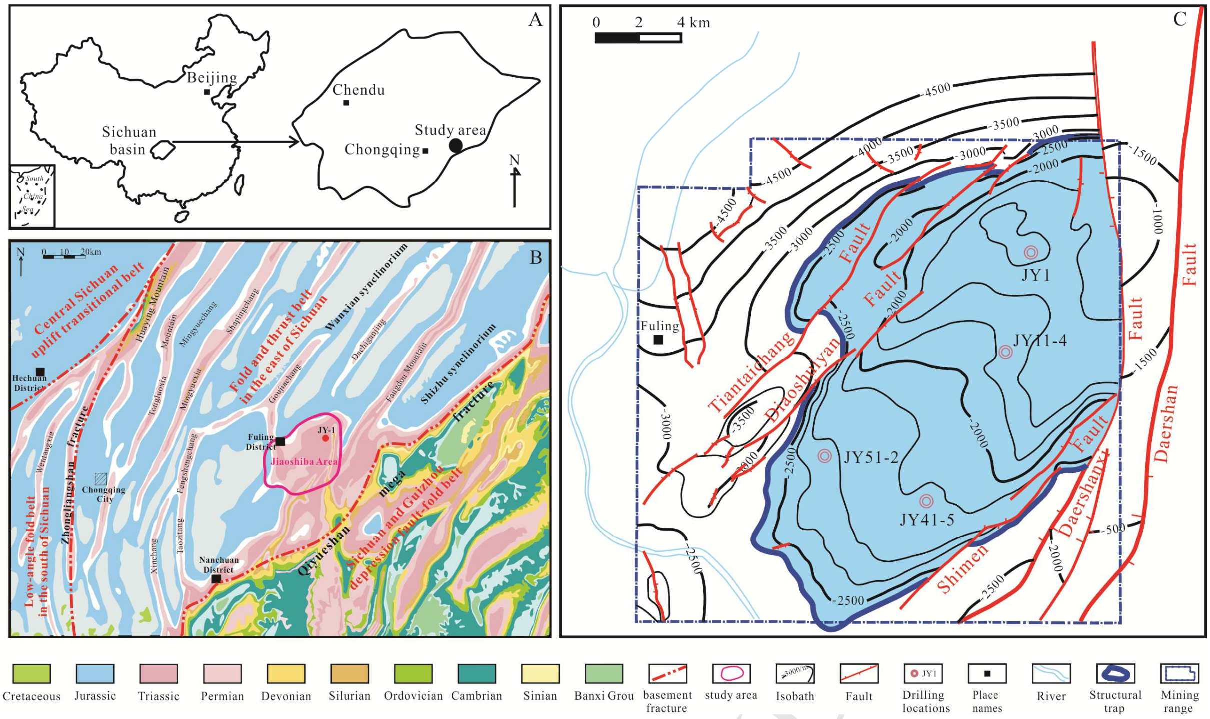
A
Beijing
Sichuan
basin
Chendu
Chongqing
Study area
N
B
N
Central Sichuan
uplift transitional belt
Fold and thrust belt
in the east of Sichuan
Wanxian synclinorium
Shizhu synclinorium
Hechuan
District
Fuling
District
JY-1
Jiaoshiba Area
Chongqing
City
Nanchuan
District
Zhongliangshan
fracture
Low-angle fold belt
in the south of Sichuan
Qiyueshan
mega
fracture
Sichuan and Guizhou
depression fault-fold belt
C
0 2 4 km
Fuling
Tiantaichang
Fault
Diaoshuiyan
Fault
JY1
JY11-4
JY51-2
JY41-5
Shimen
Fault
Daershanxi
Daershan
Fault
Fault
-4500
-4000
-3500
-3000
-2500
-2000
-1500
-1000
-500
Cretaceous
Jurassic
Triassic
Permian
Devonian
Silurian
Ordovician
Cambrian
Sinian
Banxi Grou
basement
fracture
study area
Isobath
Fault
Drilling
locations
Place
names
River
Structural
trap
Mining
range

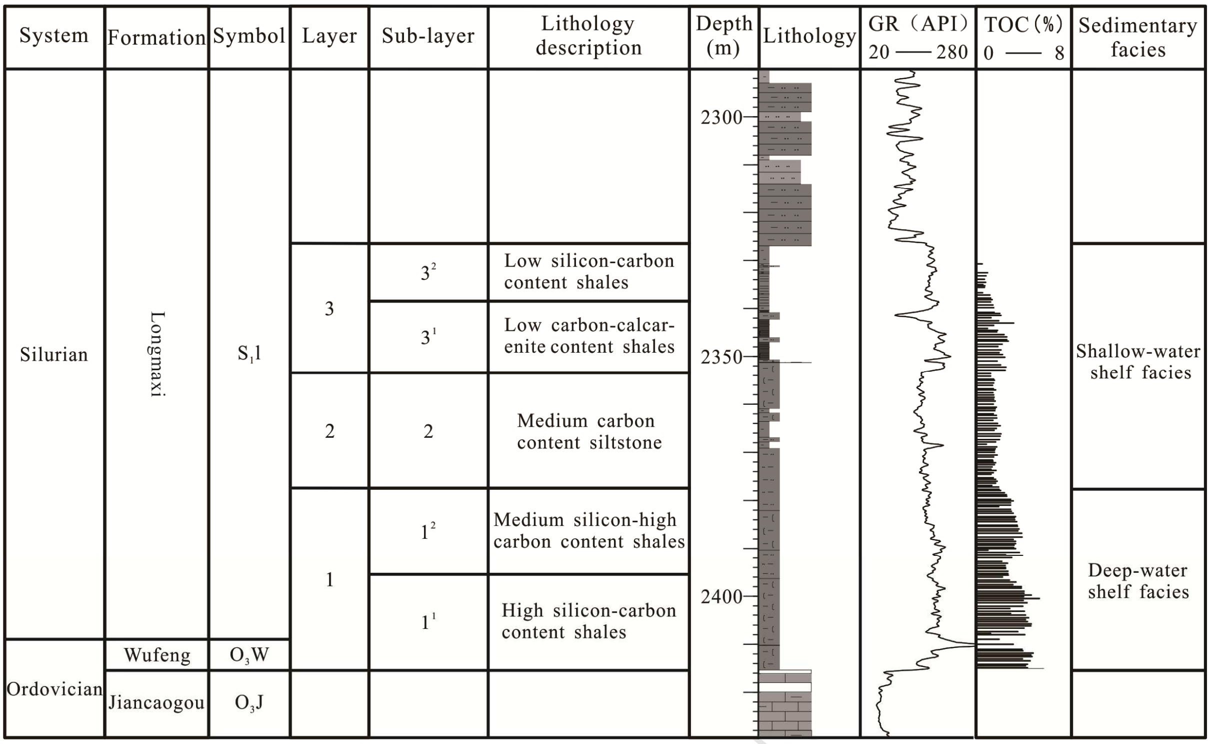
System
Formation
Symbol
Layer
Sub-layer
Lithology description
Depth (m)
Lithology
GR (API) 20 —— 280
TOC (%) 0 —— 8
Sedimentary facies
Silurian
Longmaxi
S1l
3
3²
Low silicon-carbon content shales
3¹
Low carbon-calcarenite content shales
2
2
Medium carbon content siltstone
1
1²
Medium silicon-high carbon content shales
1¹
High silicon-carbon content shales
Ordovician
Wufeng
O3W
Jiancaogou
O3J
2300
2350
2400
Shallow-water shelf facies
Deep-water shelf facies

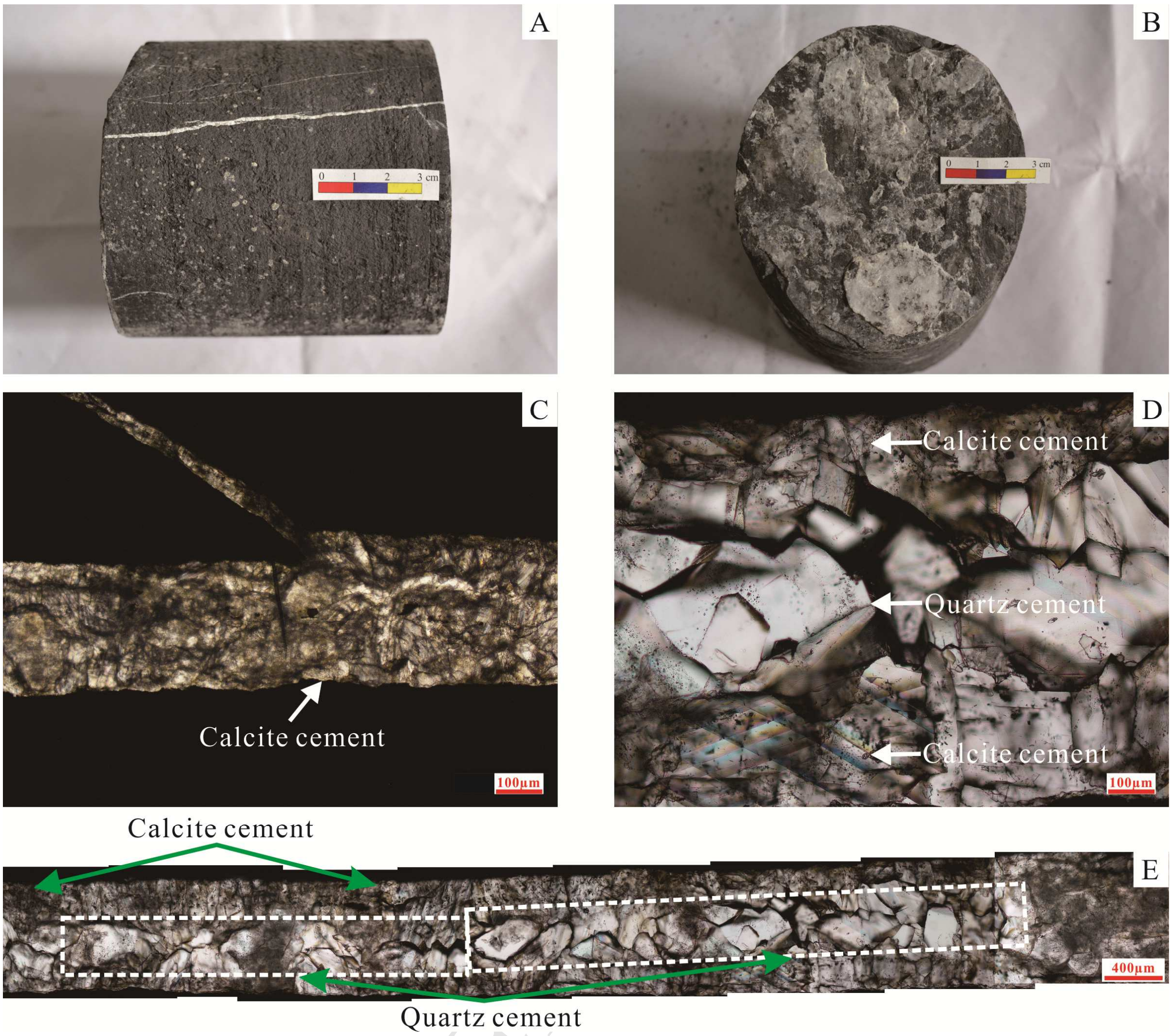
A
0 1 2 3 cm
B
0 1 2 3 cm
C
Calcite cement
100μm
D
Calcite cement
Quartz cement
Calcite cement
100μm
Calcite cement
E
400μm
Quartz cement

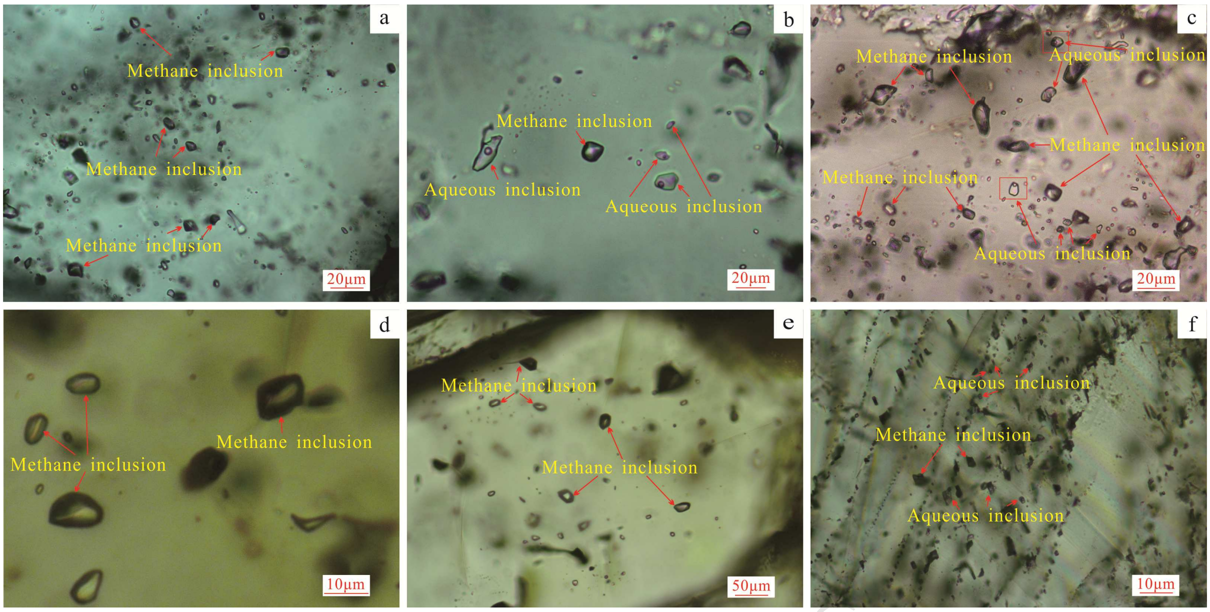
a
Methane inclusion
Methane inclusion
Methane inclusion
20μm
b
Methane inclusion
Aqueous inclusion
Aqueous inclusion
20μm
c
Methane inclusion
Aqueous inclusion
Methane inclusion
Methane inclusion
Aqueous inclusion
20μm
d
Methane inclusion
Methane inclusion
10μm
e
Methane inclusion
Methane inclusion
50μm
f
Aqueous inclusion
Methane inclusion
Aqueous inclusion
10μm

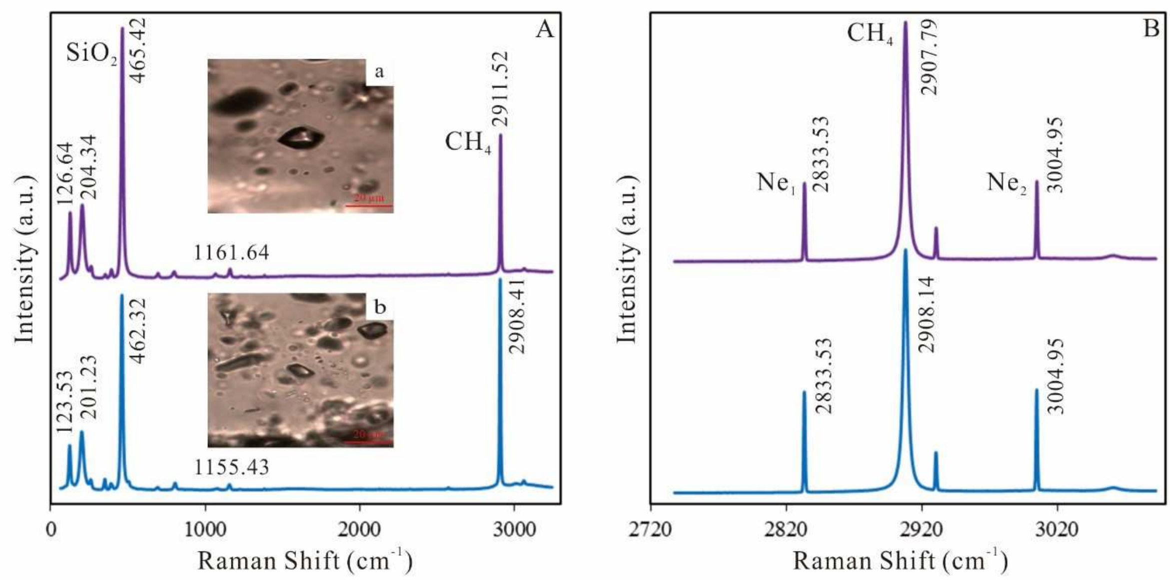
A
SiO$_2$
465.42
126.64
204.34
CH$_4$
2911.52
1161.64
a
b
462.32
123.53
201.23
2908.41
1155.43
Intensity (a.u.)
Raman Shift (cm^{-1})
0
1000
2000
3000
B
CH$_4$
2907.79
Ne$_1$
2833.53
Ne$_2$
3004.95
2908.14
2833.53
3004.95
2720
2820
2920
3020

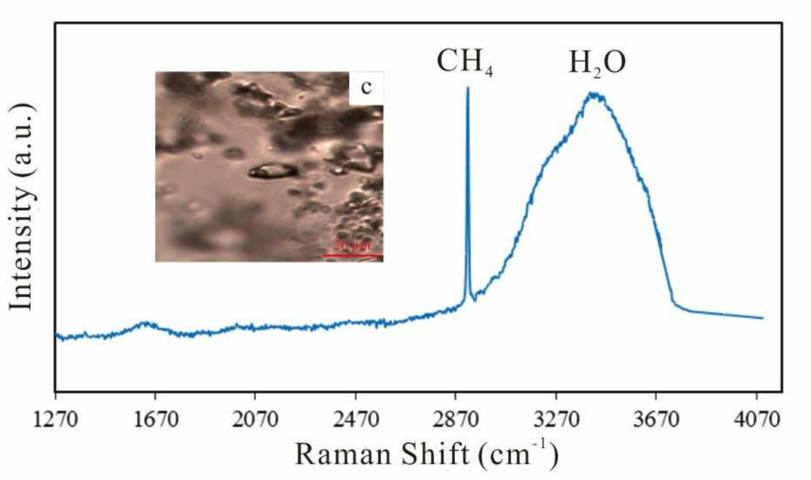
CH4
H2O
c
Intensity (a.u.)
1270
1670
2070
2470
2870
3270
3670
4070
Raman Shift (cm-1)

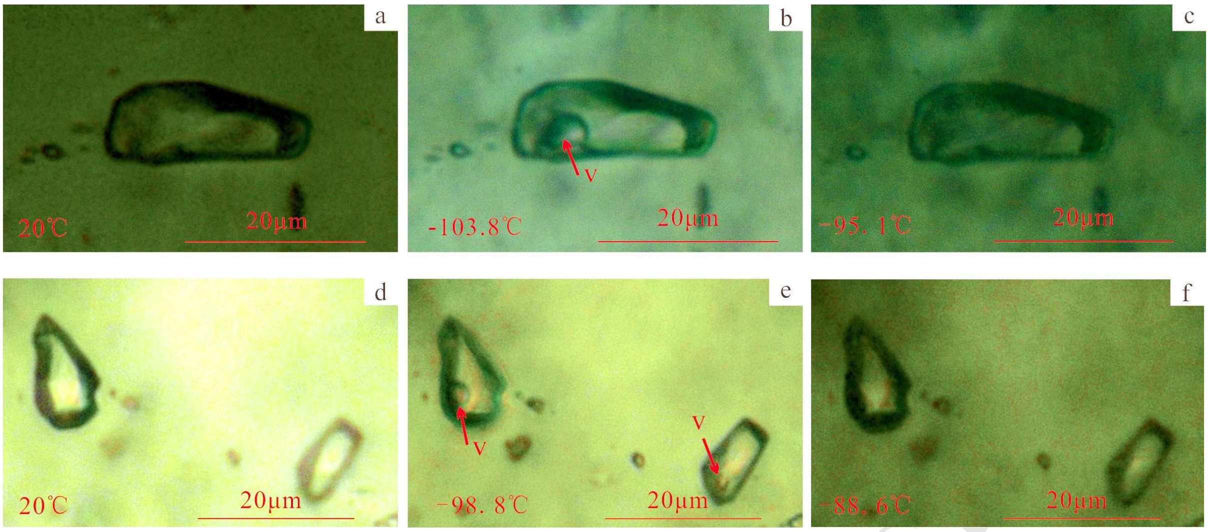
a
b
c
d
e
f
20℃
-103.8℃
-95. 1℃
20℃
-98. 8℃
-88. 6℃
20μm
v

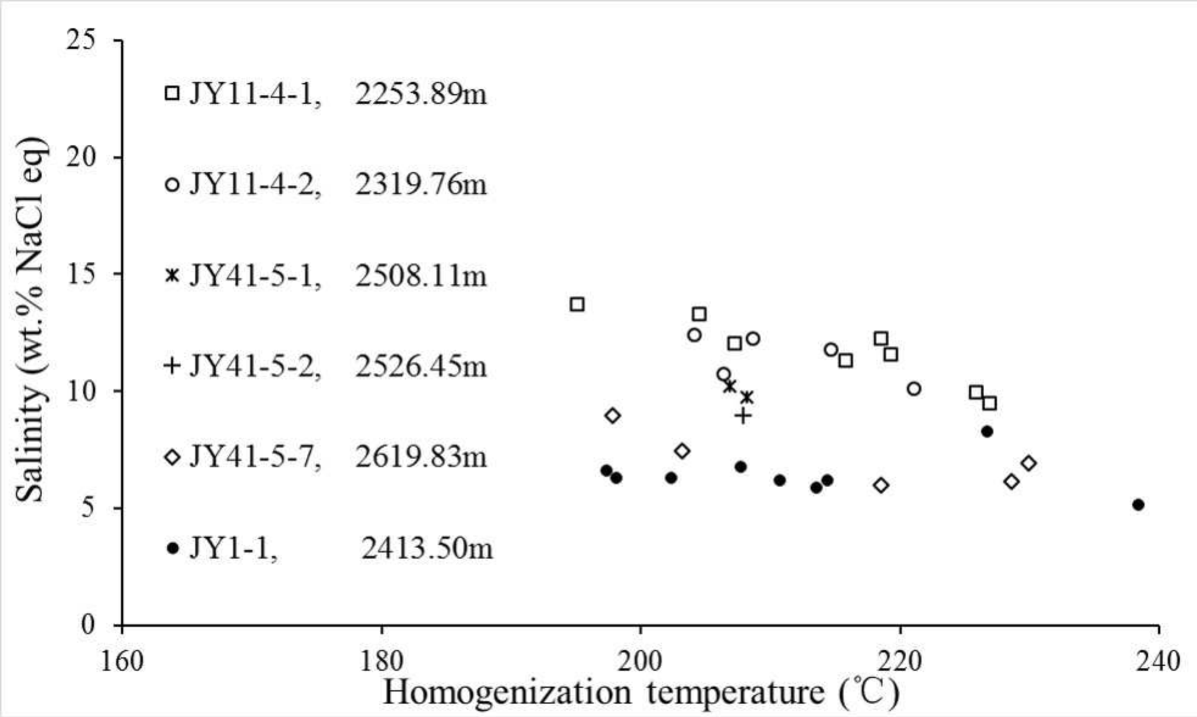
Salinity (wt.% NaCl eq)
Homogenization temperature (℃)
JY11-4-1, 2253.89m
JY11-4-2, 2319.76m
JY41-5-1, 2508.11m
JY41-5-2, 2526.45m
JY41-5-7, 2619.83m
JY1-1, 2413.50m
0
5
10
15
20
25
160
180
200
220
240

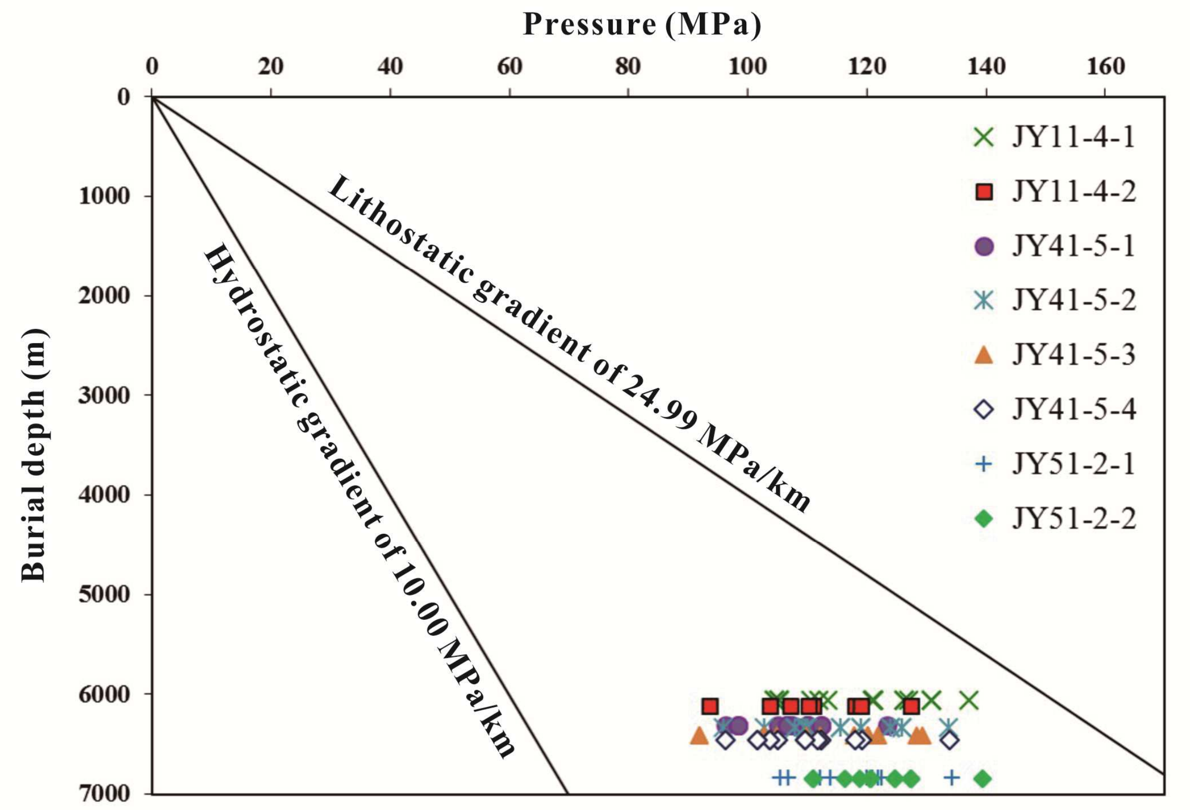

Pressure (MPa)
0
20
40
60
80
100
120
140
160
Burial depth (m)
0
1000
2000
3000
4000
5000
6000
7000
Lithostatic gradient of 24.99 MPa/km
Hydrostatic gradient of 10.00 MPa/km
JY11-4-1
JY11-4-2
JY41-5-1
JY41-5-2
JY41-5-3
JY41-5-4
JY51-2-1
JY51-2-2

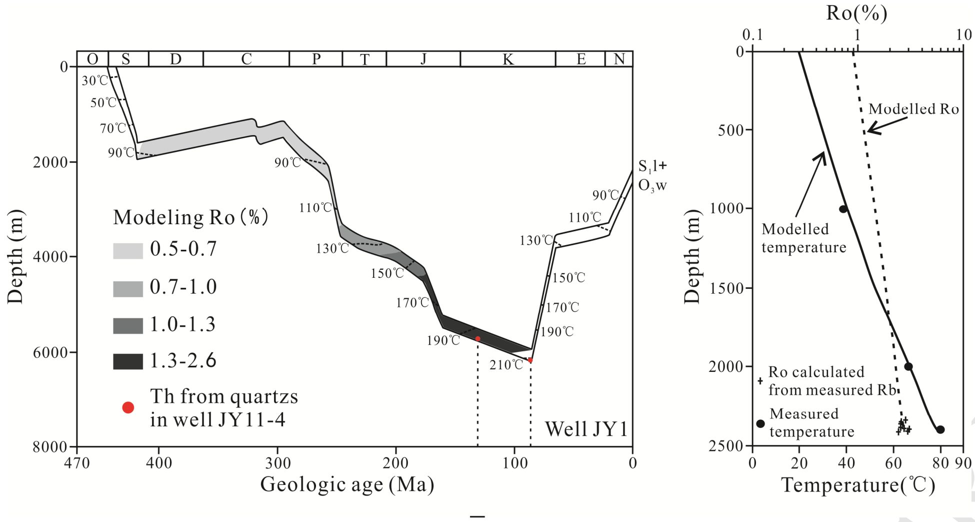
O S D C P T J K E N
Depth (m)
Geologic age (Ma)
Modeling Ro (%)
0.5-0.7
0.7-1.0
1.0-1.3
1.3-2.6
Th from quartzs in well JY11-4
Well JY1
S1l+ O3w
Ro(%)
Modelled Ro
Modelled temperature
Ro calculated from measured Rb
Measured temperature
Temperature(℃)

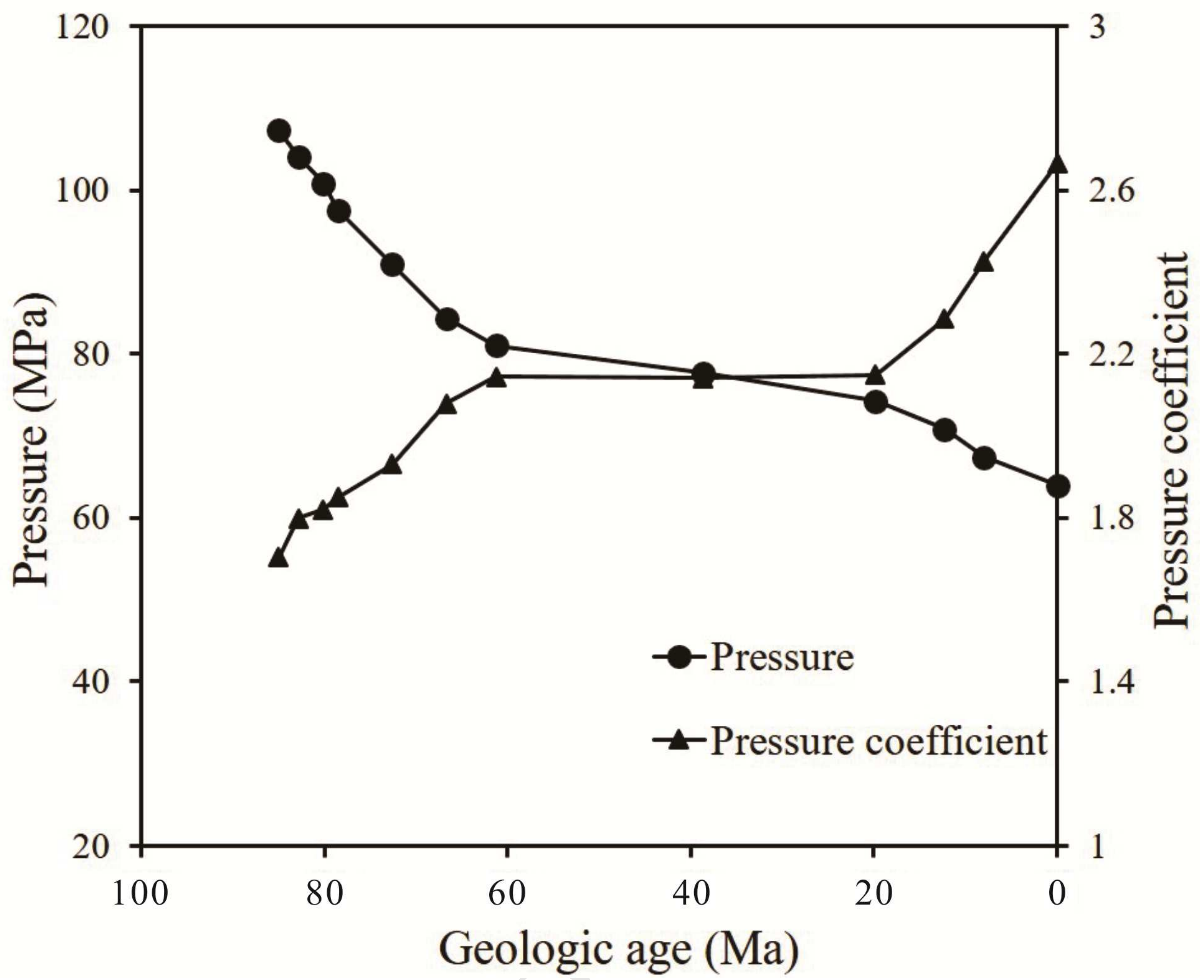

120
100
80
60
40
20
Pressure (MPa)
3
2.6
2.2
1.8
1.4
1
Pressure coefficient
Pressure
Pressure coefficient
100
80
60
40
20
0
Geologic age (Ma)

Highlights

1. Raman shift of C-H symmetric stretching (v_1) band of methane is used to calculate the density of methane inclusions

2. The trapping pressures of methane inclusions are calculated on the basis of the equations of state for supercritical methane

3. Constrain and reconstruct paleo-pressures and paleo-temperatures during the post-depositional history of the Jiaoshiba gas shale formations from fluid inclusions

4. Demonstrate that the cause of present-day overpressure in shale gas deposits is actually preservation of moderate-high overpressure developed as a result of gas generation.